Effects of free-stream turbulence on rough surface turbulent boundary layers

BRIAN BRZEK[1], SHEILLA TORRES-NIEVES[1],
JOSÉ LEBRÓN[1], RAÚL CAL[2], CHARLES MENEVEAU[2]
AND LUCIANO CASTILLO[1]†

[1]Department of Mechanical Aeronautical and Nuclear Engineering, Rensselaer Polytechnic Institute, Troy, NY 12180, USA

[2]Department of Mechanical Engineering, The Johns Hopkins University, Baltimore, MD 21250, USA

Several effects of nearly isotropic free-stream turbulence in transitionally rough turbulent boundary layers are studied using data obtained from laser Doppler anemometry measurements. The free-stream turbulence is generated with the use of an active grid, resulting in free-stream turbulence levels of up to 6.2 %. The rough surface is characterized by a roughness parameter $k^+ \approx 53$, and measurements are performed at Reynolds numbers of up to $Re_\theta = 11\,300$. It is confirmed that the free-stream turbulence significantly alters the mean velocity deficit profiles in the outer region of the boundary layer. Consequently, the previously observed ability of the Zagarola & Smits (*J. Fluid Mech.*, vol. 373, 1998, p. 33) velocity scale $U_\infty \delta^*/\delta$ to collapse results from both smooth and rough surface boundary layers, no longer applies in this boundary layer subjected to high free-stream turbulence. In inner variables, the wake region is significantly reduced with increasing free-stream turbulence, leading to decreased mean velocity gradient and production of Reynolds stress components. The effects of free-stream turbulence are clearly identifiable and significant augmentation of the streamwise Reynolds stress profiles throughout the entire boundary layer are observed, all the way down to the inner region. In contrast, the Reynolds wall-normal and shear stress profiles increase due to free-stream turbulence only in the outer part of the boundary layer due to the blocking effect of the wall. As a consequence, there is a significant portion of the boundary layer in which the addition of nearly isotropic turbulence in the free-stream, results in significant increases in anisotropy of the turbulence. To quantify which turbulence length scales contribute to this trend, second-order structure functions are examined at various distances from the wall. Results show that the anisotropy created by adding nearly isotropic turbulence in the free-stream resides mostly in the larger scales of the flow. Furthermore, by analysing the streamwise Reynolds stress equation, it can be predicted that it is the wall-normal gradient of $\langle u^2 v \rangle$ term that is responsible for the increase in $\langle u^2 \rangle$ profiles throughout the boundary layer (i.e. an efficient turbulent transport of turbulence away from the wall). Furthermore, a noticeable difference between the triple correlations for smooth and rough surfaces exists in the inner region, but no significant differences are seen due to free-stream turbulence. In addition, the boundary layer parameters δ^*/δ_{95}, H and c_f are also evaluated from the experimental data. The flow parameters δ^*/δ_{95} and H are found to increase due to roughness, but decrease due to free-stream turbulence, which has significance for flow control, particularly in delaying separation. Increases

† Email address for correspondence: castil2@rpi.edu

in c_f due to high free-stream turbulence are also observed, associated with increased momentum flux towards the wall.

---

1. Introduction

The study of how external conditions (i.e. inlet conditions, external pressure gradient, surface roughness, free-stream turbulence, etc.) influence turbulent boundary layers is important since such effects are often present in common engineering applications. They can also be exploited for flow control, and they provide variations about standard smooth-wall boundary layers that provide insightful tests for turbulence models. Figure 1 illustrates some of the external conditions that can be present in boundary layers. The left side of the region involves the inlet or upstream conditions including the upstream velocity U_o, free-stream turbulence Tu_∞ and different tripping conditions of the boundary layer such as location L_o and diameter d_o. The top and bottom surfaces involve the lower wall (including surface roughness k^+) and outer boundary conditions (e.g. imposed external pressure gradient η_p). As the boundary layer begins to develop, the interaction with the wall boundary condition introduces new length and time scales. The dominant scales in the flow depend on the nature of the different external conditions, as well as the downstream development, as some of the effects of initial scales may decay or die out, (i.e. trip-wire effects, free-stream turbulence decay). When multiple external conditions are present, multiple length and time scales may be important. Different applications such as gas turbine blade aerodynamics, heat exchangers, wind turbines, urban aerodynamics and underwater bodies involve widely different levels of free-stream turbulence, surface roughness and range of relevant scales.

Surface roughness has been studied extensively given its importance in high Reynolds number flows where the viscous region of the boundary layer becomes thinner, thereby making it more susceptible to wall roughness. Many researchers followed the 'attached eddy' hypothesis of Townsend (1976); all mean relative motions and energy-containing components of the turbulent motions are independent of viscosity and surface roughness. Consequently, at a high Reynolds number, the smooth and rough velocity profiles are similar in the outer region. Jiménez (2004) provides a further constraint on this hypothesis where the Reynolds number must be large (i.e. at least large enough for an inertial subrange to exist) and the ratio of roughness height k to boundary layer thickness δ is small, $k/\delta < 0.02$. Furthermore, the 'attached eddy' hypothesis is based on the assumption that a single velocity may be used for scaling, and that this may be applied for smooth and rough surfaces. This hypothesis is supported by the investigations of Perry & Li (1990), Schultz & Flack (2003) and Schultz & Flack (2005), among others. Akinlade *et al.* (2004), Tachie, Bergstrom & Balachandar (2000, 2003) and Krogstad & Antonia (1999) have also presented evidence contradicting the attached eddy hypothesis. Many of these differences revolve around the importance of roughness geometry and the ratio k/δ.

Many investigations with high free-stream turbulence focused on its role in the transition from laminar to turbulent flow in practical engineering applications, (e.g. Radmsky & Thole 2002; Roberts & Yaras 2005). These studies were carried out for conditions replicating those found on turbine blades. Other investigations showed the importance of high free-stream turbulence on heat transfer in turbulent boundary layers. Thole & Bogard (1995) investigated the increase in heat transfer due to high
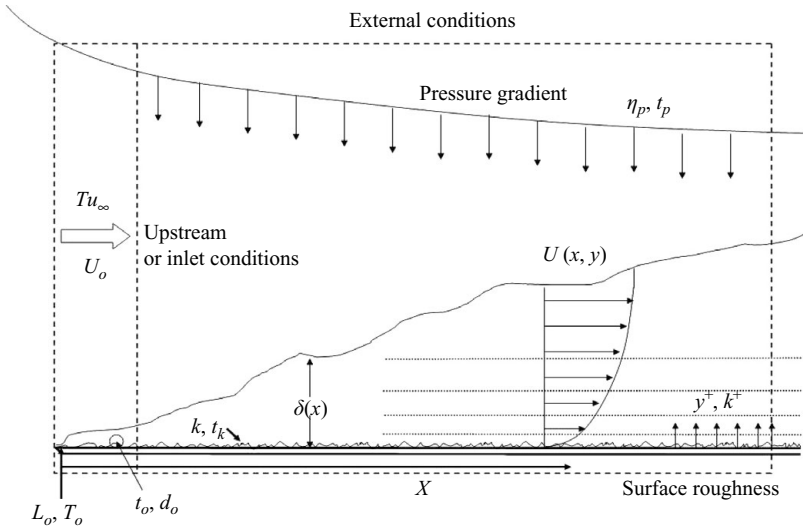
FIGURE 1. A boundary layer subjected to different external conditions.

free-stream turbulence, as well as various correlations used to predict this increase. Barrett & Hollingsworth (2003b, c) studied the effects of turbulence intensity and integral length scales on heat transfer and skin friction, along with various correlations for low Reynolds number ($Re_\theta < 2700$) smooth surface zero-pressure-gradient (ZPG) boundary layers. Castro (1984) also examined the effects of free-stream turbulence on low Reynolds number ($Re_\theta < 2500$) turbulent boundary layers and found that high free-stream turbulence decreased the amount of Reynolds number dependence in the Reynolds stress distributions. In the same study, different correlations predicting the increase in wall shear stress due to high free-stream turbulence were also examined. Furthermore, Bandyopadhyay (1992) showed two effects of low Reynolds numbers on the outer flow. The first was that Clauser's shape parameter G is Reynolds number dependent at low Reynolds numbers. The second was that the reduction in the wake component due to free-stream turbulence undergoes a reversal in the Reynolds number dependence, depending on the value of the free-stream turbulence parameter.

One important characteristic of high free-stream turbulence intensity is an increase in the skin friction coefficient c_f as pointed out by Hancock & Bradshaw (1983). Many investigations have tried to relate properties of the free-stream turbulence to the increase in skin friction. For instance, Hancock & Bradshaw showed that the increase in c_f is affected by both the free-stream turbulence intensity Tu_∞ and the ratio of the free-stream turbulent integral scale to boundary layer thickness L_∞/δ. From their experimental data, a correlation was developed to predict the increase in skin friction from information about the free-stream turbulence intensity and integral scale. Blair (1983) used this correlation and added an extra 'damping' term to account for low Reynolds number effects. From this correlation, the change in c_f due to high free-stream turbulence, $\Delta c_f/c_{fo} = (c_f - c_{fo})/c_{fo}$, can be computed where c_f is the value of the skin friction for smooth surfaces with high free-stream turbulence, and c_{fo} is the value without free-stream turbulence. This correlation must compare boundary layers at a fixed Reynolds number, i.e. Re_θ. Stefes & Fernholz (2004) carried out direct measurements of the skin friction using oil-film interferometry and showed reasonable agreement with the Blair (1983) correlation for cases with high free-stream turbulence. Barrett & Hollingsworth (2003a, c) also correlated the increase

in skin friction with various free-stream properties, and developed correlations for the increase in heat transfer.

The effect of high free-stream turbulence on the velocity and Reynolds stress profiles was also explored by Hancock & Bradshaw (1983), Thole & Bogard (1996), as well as others. These investigations showed that high free-stream turbulence drastically reduces the Coles (1962) wake parameter Π for ZPG boundary layers, even to negative values. They also studied the validity of the logarithmic region in the overlap region when high free-stream turbulence intensity is present. Blair (1983) showed that for $Tu_\infty < 5.2\,\%$ and $Re_\theta \approx 3,000$, the profiles exhibited a logarithmic region between $30 < y^+ < 200$. Hancock & Bradshaw (1983) showed evidence of a logarithmic region but Stefes & Fernholz (2004) showed that it degraded rapidly with increasing turbulence intensity for low Reynolds number flows.

Thole & Bogard (1996) showed that for $Tu_\infty > 20\,\%$, the entire streamwise Reynolds stress profiles were affected by free-stream turbulence, and the value near the wall was equal to that of the free-stream level. For the wall-normal component, the vertical fluctuations were attenuated by the wall and grew as the free stream is approached. However, these measurements were restricted to Reynolds numbers of less than $Re_\theta < 1150$. Stefes & Fernholz (2004) showed self-similarity in the streamwise Reynolds stress below $y^+ < 10$ even with high free-stream turbulence. However, beyond $y^+ > 10$, there was a considerable increase due to free-stream turbulence. For the wall-normal component, similarities were seen near the wall but free-stream turbulence increased the wall-normal fluctuations farther from the wall. Hancock & Bradshaw (1989) showed in detail the diffusion of turbulent kinetic energy, as well as a complete balance of the turbulent kinetic energy equations. The data given by Hancock & Bradshaw (1989) included a significant range of L_∞/δ and Tu_∞ for smooth surface ZPG flows at Reynolds numbers below $Re_\theta < 5800$. Furthermore, the Reynolds stress profiles and triple products were shown to be strongly affected by free-stream turbulence. Aronson, Johansson & Löfdahl (1996) showed the effects of free-stream turbulence in a shear free wall bounded flow. Their results indicate that two different length scales are associated with the near wall damping of the Reynolds stresses. Furthermore, the wall-normal Reynolds stress is damped over a region extending one macroscale out from the wall.

One of the important aspects of high free-stream turbulence is how it is generated. Many investigations use passive grids while others use active techniques. For instance, Stefes & Fernholz (2004) and Thole & Bogard (1996) used air jets injected perpendicularly to the main flow field, whereas Hancock & Bradshaw (1989) and Blair (1983) used square bar arrays. This resulted in a wide range of different free-stream turbulence intensities, integral length scales and levels of isotropy. A limitation of many investigations is that they have been for relatively low Reynolds numbers (i.e. $Re_\theta < 2000$–4000) where there is not much separation between the large and small scales of turbulence, and no true inertial region exists (George & Castillo 1997). Up to now, no experimental studies have focused on the effects of high free-stream turbulence intensity on a rough surface ZPG turbulent boundary layer, at relatively high Reynolds numbers (i.e. $5939 \leqslant Re_\theta \leqslant 11\,319$).

Therefore, the main goal of this experimental investigation is to study the effects of high free-stream turbulence on the behaviour of rough surface turbulent boundary layers, at relatively high Reynolds numbers for laboratory experiments. In particular, several issues will be addressed including scaling of mean velocity profiles, the penetration mechanisms of the free-stream turbulence into the boundary layer turbulence and what scales of motion dominate these mechanisms, and effects on the
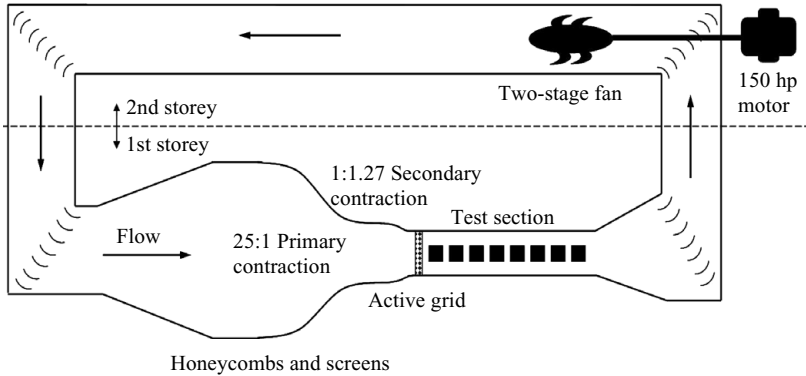
FIGURE 2. Stanley Corrsin Wind Tunnel Facility.

resulting turbulence anisotropy. At relevant places, the measurements are compared to the smooth surface data of DeGraaff & Eaton (2000), Österlund (1999), as well as the rough surface measurements of Brzek *et al.* (2007) without free-stream turbulence. Furthermore, the smooth wall data with high free-stream turbulence from Hancock & Bradshaw (1989) are used to complement the present results.

2. Experimental set-up

Experiments were performed in the Corrsin Wind Tunnel Facility at Johns Hopkins University. The wind tunnel is closed loop, with primary and secondary contractions with ratios of 25:1 and 1.27:1, respectively, leading into the test section. The test section dimensions are 1.22 m wide by 0.91 m high with a length of 10 m. Figure 2 shows a schematic of the wind tunnel facility along with the major dimensions. To create the boundary layer, a custom made flat plate was constructed from medium density fibreboard, which consisted of eleven segments, each with a length of 0.6 m. The leading edge was a 3:1 elliptical profile. The flat plate was 19 mm thick and extended the width of the test section. When assembled, the plate was 6.7 m long with the leading edge approximately 1.05 m from the end of the secondary contraction. For the smooth case, a cylindrical trip-wire of 1.6 mm in diameter was placed 10 cm from the leading edge and spanned the width of the test section, resulting in a Reynolds number based on diameter of 1600.

For the rough surface cases, a continuous sheet of 24 grit aluminum oxide, heavy grit sand paper was used. The plate was covered by the 900 mm wide sheet of sand paper running around the leading edge, and all the way to the trailing edge of the plate. The sheet of sand paper was attached to the plate using double-sided tape covering the majority of the surface. Measurements of the roughness characteristics were performed by an independent laboratory and the statistical parameters are summarized in table 1. For these results, S_a is the arithmetic mean deviation of the surface, S_q is the root mean square (r.m.s.) deviation of the surface, S_t is the height between the highest peak and deepest valley, S_p is the height between the highest peak and mean plane, S_v is the depth between the mean plane and the deepest valley, and S_z is the ten-point height, which is the average of the five highest peaks and five deepest valleys. As in Brzek *et al.* (2007), the roughness height quoted in this investigation k is taken to be the ten-point height S_z, since according to Bradshaw (2000), the contribution of the larger peaks is significant compared to the smaller

Surface	S_a (mm)	S_q (mm)	S_t (mm)	S_p (mm)	S_v (mm)	S_z (mm)
24 grit	0.202	0.248	1.579	1.001	0.577	1.522

TABLE 1. Statistical parameters of 24 grit sand paper.

(a)

Three-dimentional characterization of the 24 grit surface

(b)

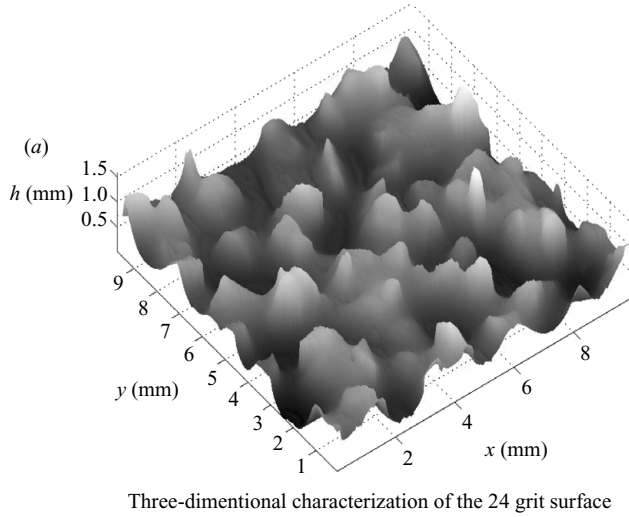Probability density function of roughness heights for the 24 grit surface
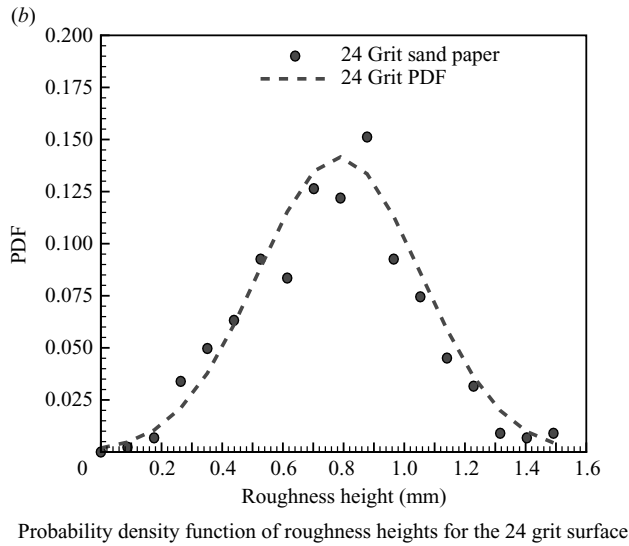
FIGURE 3. The 24 grit surface.

peaks. A three-dimensional visualization of a portion of the surface is given in figure 3(a). Figure 3(b) shows the measured probability density function of the height of the roughness peaks. The results show that the roughness element heights follow a normal distribution quite closely.

The free-stream turbulence was generated using an active grid (AG), with a configuration including diamond-shaped winglets, as proposed by Mydlarski &

(a)

Motor 6 Motor 7 Motor 8 Motor 9 Motor 10 Motor 11 Motor 12

Motor 5

Motor 4

Motor 3

Motor 2

Motor 1

Horizontal shaft

Vertical shaft

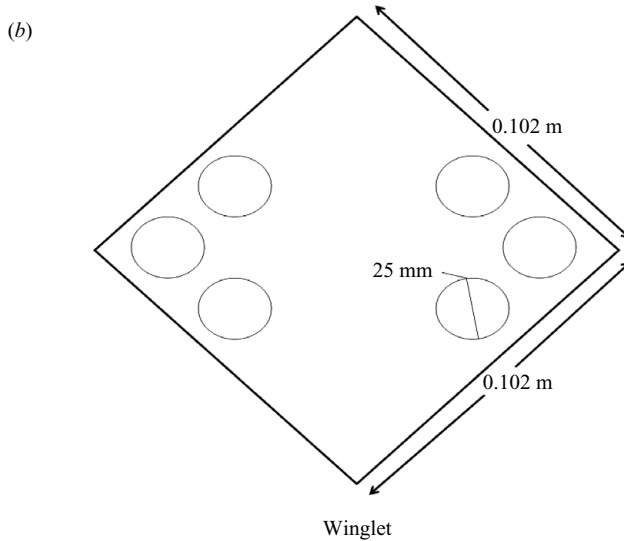Active grid schematic
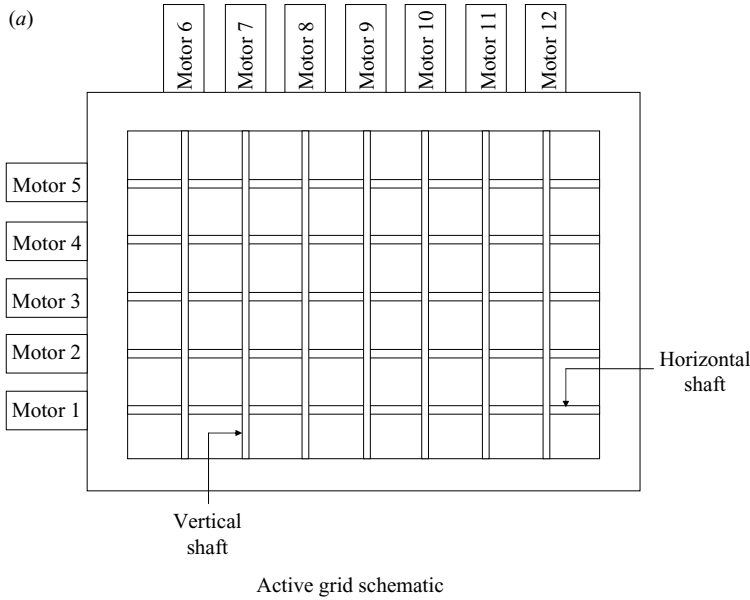
(b)

0.102 m

25 mm

0.102 m

Winglet

FIGURE 4. The active grid.

Warhaft (1996). The set-up was the same as implemented and documented in Kang, Chester & Meneveau (2003) for their remake of the classical turbulence decay experiment of Comte-Bellot & Corrsin (1966). AGs have the benefit of providing free stream turbulence with a much larger Reynolds number based on Taylor microscale than passive grids. The AG consisted of five horizontal and seven vertical shafts, each connected to an independently driven 1/4 hp AC motor (Baldor Industrial Motor, CNM20252). A schematic of the AG mounted in the test section is shown in figure 4(a). Each motor was independently controlled and programmed to change its speed and direction once every second. The rotational speed varied randomly between 210 and 420 r.p.m., in both directions (i.e. clockwise and counter-clockwise).

Additional information about the AG can be found in Kang *et al.* (2003). The agitator winglets connected to the shafts were 3.18 mm thick and 0.102 m by 0.102 m wide. Each winglet had six holes, each with a diameter of 25 mm as depicted in figure 4(*b*). Eight winglets were attached to the horizontal shaft and six winglets were attached to the vertical shaft. The AG was located at the end of the secondary contraction, and 1.05 m in front of the leading edge of the plate on which the boundary layer develops.

A two-dimensional laser Doppler anemometry (LDA) probe was placed nearly horizontal at the side of the wind tunnel. This probe emitted four beams of blue (488 nm) and green (514.5 nm) light from a Spectra Physics ion laser. One expander with an expansion ratio of 1.94:1 was used with focusing optics with a focal length of 600 mm. Using back-scatter mode, the measuring control volume had a diameter of 147 μm. To avoid blockage of the wall-normal component, the probe was tilted approximately $3.5°$, so that measurements could be performed at the wall. Due to the smallness of the angle of rotation and the small spanwise velocity component, no correction of the vertical velocity component was performed (see e.g. DeGraaff & Eaton 2001 for the relevant analysis and recommendations). The effect of the rotation, especially on the cross-correlations $-\langle uv \rangle$, is expected to be negligible except near the wall, where it still falls within the quoted overall uncertainty of the data.

Finding the wall position in rough surfaces is challenging, thus a smooth piece of Plexiglas with a constant thickness of $t = 2.75$ mm was placed on top of the surface. The glass piece was large enough such that it rested on top of roughness elements with approximately the same height. The LDA probe volume was positioned precisely on the top surface of the glass, and then traversed towards the wall the exact thickness of the glass. This was then recognized as the reference zero position of the surface (i.e. the top of the highest roughness elements). The adjustment for the virtual origin ϵ, which is required for rough surfaces, was implemented based on the technique of Schultz & Flack (2003). The controller for the traversing mechanism has a relative position error of approximately 10–15 μm.

A Rosco fog generator located in the diffuser part of the wind tunnel produced droplets with a mean droplet size of 0.8 μm. The flow was continuously seeded to obtain consistency in data rates and validation. The data were collected for up to 400 s at each point, and between 4000 and 20 000 samples were acquired. The number of samples was strongly affected by wall proximity and seeding density. The seeding generator was difficult to control and maintain a constant seeding density. Thus, the total number of samples taken in the 400 s of data sampling varied. Furthermore, when measurements were being performed near the wall the seeding density was naturally lower and resulted in less samples. The values of 4000–20 000 are a good representation of the range in samples, although the vast majority was above 10 000. Based on the number of samples and the measured variance of the fluctuating velocities, measurement error for the mean velocity U is less than 1 %, and for the Reynolds stresses, the error is estimated to be less than 2 %.

For all cases, a nominal wind tunnel speed of $U_o = 10 \text{ m s}^{-1}$ was used, so that the measurements could be compared with those of Brzek *et al.* (2007) which used similar experimental conditions (i.e. wind tunnel speed, roughness). Measurements were taken at two downstream locations with and without the AG, such that the downstream development could be compared. These locations were at $x = 3.15$ m and $x = 4.76$ m from the leading edge of the plate and are referred to as $L1$ and $L2$, respectively.

Case	x (m)	U_∞ (m s^{-1})	u_τ (m s^{-1})	δ_{99} (m)	δ_{95} (m)	θ (m)	$\delta^*(m)$	L_∞ (m)
JHU smooth	4.76	10.0	0.37	0.072	0.057	0.0089	0.0124	NA
JHU rough $L1$	3.15	10.2	0.49	0.074	0.059	0.0102	0.0155	NA
JHU rough $L2$	4.76	10.0	0.47	0.094	0.080	0.0131	0.0196	NA
JHU rough $L1$ AG	3.15	9.8	0.53	0.138	0.073	0.0114	0.0154	0.136
JHU rough $L2$ AG	4.76	10.4	0.53	0.181	0.105	0.0162	0.0221	0.157

TABLE 2. Dimensional parameters of five data sets.

Case	Re_θ	δ^+	k/δ_{99}	k^+	c_f	Π	$Tu_\infty(\%)$	L_∞/δ_{99}	L_∞/η_{k_∞}
JHU smooth	5939	1791	0	0	0.0028	0.70	NA	NA	NA
JHU rough $L1$	6954	2440	0.02	50	0.0047	0.70	NA	NA	NA
JHU rough $L2$	8733	2993	0.016	48	0.0046	0.66	NA	NA	NA
JHU rough $L1$ AG	7427	4828	0.011	53	0.0058	−0.10	6.2	0.97	620
JHU rough $L2$ AG	11 319	6455	0.0083	54	0.0053	0.02	5.2	0.87	635

TABLE 3. Non-dimensional parameters of various data sets.

The integral length scale of the free-stream turbulence was evaluated (Mydlarski & Warhaft 1996) using (2.1):

$$L_\infty \approx 0.9 \frac{u_\infty'^3}{\varepsilon}, \tag{2.1}$$

where ε is the dissipation rate and u_∞' is the r.m.s. velocity in the free stream. This approximation becomes increasingly accurate as the turbulent Reynolds number increases beyond $L_\infty/\eta_{k_\infty} > 10^4$, where $\eta_{k_\infty} = (\nu^3/\varepsilon)^{(1/4)}$ is the Kolmogorov length scale in the free stream. This condition is not satisfied in the present investigation since $L_\infty/\eta_{k_\infty} \approx 630$, (see table 3), thus (2.1) can only be used as an approximation. Due to the uneven time intervals of the LDA sampling and spatial resolution, the dissipation rate in the free stream was computed using the second-order structure function approach as described in §5.4.1. This technique provides a good estimate of the dissipation rate ε, and, using (2.1), of the free-stream integral scale L_∞.

The dimensional parameters of the five data sets are listed in table 2, where δ_{99} is the height from the wall at which the local velocity is 0.99 of the free-stream value. The values of the friction velocity shown in table 2 were obtained from the constant stress layer equation with correction for the external pressure gradient discussed in §3. Notice that the integral length scale of the free-stream turbulence is of the same order as the boundary layer. Relevant non-dimensional experimental parameters are given in table 3. They include the Reynolds number based on momentum thickness Re_θ, ratio of outer and inner length scales δ^+, ratio of roughness height to boundary layer thickness k/δ_{99}, roughness parameter k^+, skin friction coefficient c_f, Coles (1962) wake parameter Π, the free-stream turbulence intensity Tu_∞, as well as length scale ratios associated with the free-stream turbulence. As previously described, the parameter $k/\delta_{99} < 0.02$ is important when considering classical wall similarity (Jiménez 2004). This is typically achieved when the Reynolds number becomes larger than $Re_\theta > 10\,000$, since the large-scale motion is no longer affected by viscosity. In the experimental results of Brzek *et al.* (2007), this condition was not satisfied since $k/\delta_{99} > 0.02$. However, in the present investigation, the wall similarity condition is satisfied for the last case where the Reynolds number is greater than $Re_\theta > 10\,000$ and $k/\delta < 0.02$.

Case	Viscous length scale, ν/u_τ (μm)	Probe diameter/ viscous scale
JHU smooth	40	3.72
JHU rough $L1$	30	4.93
JHU rough $L2$	32	4.76
JHU rough $L1$ AG	29	5.26
JHU rough $L2$ AG	28	5.33

TABLE 4. Spatial resolution.

The value of the wake parameter Π for the different cases is calculated based on the method described in Krogstad, Antonia & Browne (1992) and compared with the method described in Blair (1983) with good agreement between the two. Using these techniques, the value of the friction velocity calculated from the constant stress method (described in §3) was used and only the value of Π was optimized. The results indicate that for these particular cases, there was little effect of roughness on the wake parameter. However, as noted in many investigations, there was a significant effect due to the free-stream turbulence. With high free-stream turbulence, the value of the wake parameter was negative for location $L1$, and approached a value of approximately zero for location $L2$.

The turbulence intensity in the free stream was evaluated as the ratio of average r.m.s. turbulence to mean velocity (defined in (2.2)),

$$Tu_\infty = \frac{\sqrt{\frac{1}{3}(1.5\langle u^2 \rangle + 1.5\langle v^2 \rangle)}}{U}, \tag{2.2}$$

at the last measured position of the wall-normal traverse $y/\delta_{99} \approx 1.4$. Most often Tu_∞ is given in percentage units. Since the third velocity component $\langle w^2 \rangle$ could not be measured, but the streamwise and wall-normal components in the free stream were nearly equal, the average of the streamwise and wall-normal fluctuations was used to estimate the variance in the third direction (leading to the 1.5 factor in (2.2)). Throughout the paper, mean velocities are denoted by capital letters, while small letters are used for the fluctuating components.

Due to the large probe volume diameter, spatial resolution was determined to play an important role when measuring mean velocity gradients, below $(y + \epsilon)^+ < 50$ for the rough surface measurements. The probe volume diameter, viscous length scale and their ratio are listed in table 4.

3. Skin friction coefficient

One of the most important parameters in turbulent boundary layers is the skin friction coefficient. Traditionally, this quantity is obtained using a modified form of the Clauser (1954) chart. This approach is based on the validity of the classical law of the wall for rough turbulent boundary layers. Using this technique for rough surfaces requires the determination of four parameters, instead of two for smooth surfaces (Krogstad *et al.* 1992), which cannot be determined independently. Furthermore, it is not completely clear whether the presence of free-stream turbulence alters the overlap region of turbulent boundary layers under the given conditions (i.e. rough surface, Reynolds number, and free-stream turbulence intensity and integral scale). Thus, this approach was not used in the present investigation.
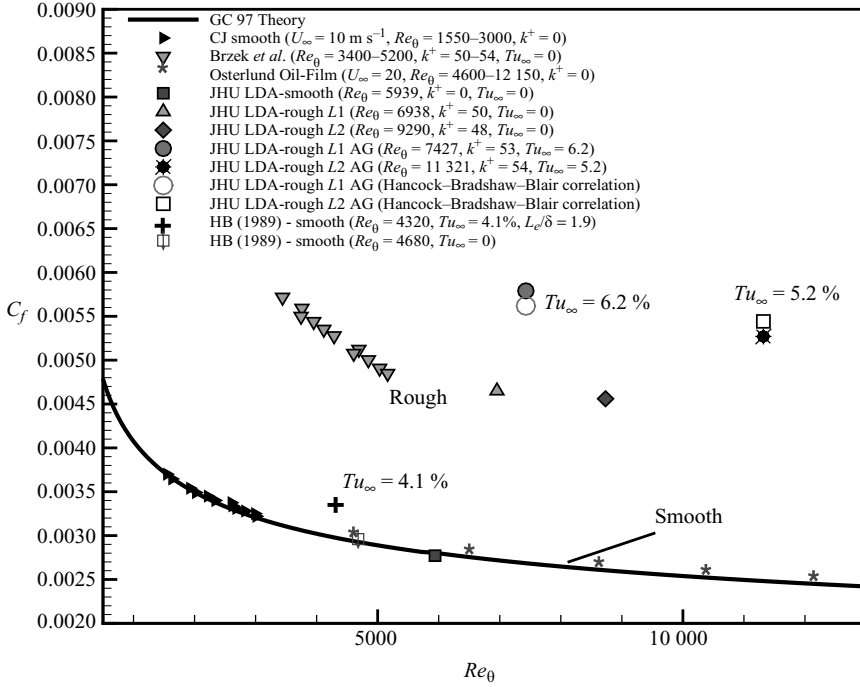
FIGURE 5. Skin friction coefficient development for smooth and rough turbulent boundary layers, with and without free-stream turbulence. Open symbols are predictions from Hancock & Bradshaw (1983) for the present measurement conditions with free-stream turbulence.

Using the integrated boundary layer equation, including all relevant terms, provides an accurate method for calculating the wall shear stress for rough surfaces (Brzek *et al.* 2007). However, in the present experiments, the x-dependence of the mean velocity and various turbulence quantities is not measured, and thus this investigation uses the approximation of a constant stress layer, but including a correction for the external pressure gradient:

$$\frac{\tau_w}{\rho} = u_\tau^2 = \nu \frac{\partial U}{\partial y} - \langle uv \rangle + U_\infty \frac{\mathrm{d}U_\infty}{\mathrm{d}x} y. \tag{3.1}$$

This coincides with the integrated full boundary layer equation in the limit as y approaches the wall, and thus is a good approximation from the wall up to approximately $(y + \epsilon)^+ = 0.1\delta^+$, and is increasingly accurate as the Reynolds number increases. For the present investigation, the Reynolds number is relatively high ($\delta^+ = 3000$–6400), and thus the mean convection terms are not expected to play a role since their contribution is less than 1 % in the inner layer (Brzek *et al.* 2008).

The pressure gradient term is kept as a correction (Castillo & Johansson 2002), since the wind tunnel walls were not adjusted to account for boundary layer growth. The x-dependence of the free-stream mean velocity required in the pressure gradient term is known due to a series of Pitot traverses in the free stream over the length of the entire plate. This term proved to be small but not negligible, e.g. at $(y + \epsilon)^+ = 0.1\delta^+$, the pressure gradient term contributed about 2.5 %.

The value of the wall shear stress was determined by averaging (3.1) between a value of $50 < (y + \epsilon)^+ < 400$. These limits also depended on which case was being examined. This was done where the errors in the near wall measurements and spatial

resolution errors prevented accurate calculations of the mean velocity gradient. The values of the wall shear stress obtained τ_w/ρ are non-dimensionalized to give the skin friction coefficient $c_f = 2\tau_w/\rho U_\infty^2$. The resulting c_f values are shown in figure 5. These data are compared to the smooth wall measurements of Österlund (1999) and Castillo & Johansson (2002), as well as the rough surface measurements of Brzek *et al.* (2007). The measurements of Brzek *et al.* (2007) were at the same external conditions (same roughness and wind tunnel speed), but at lower Reynolds numbers. They were analysed using the full integrated boundary layer equation.

The skin friction coefficient for the smooth surface was compared with the George & Castillo (1997) power law theory, and also with the oil film (direct) measurements from Österlund (1999) and Castillo & Johansson (2002) (integrated boundary layer equation). The value for the smooth surface presently obtained using (3.1) (square symbol in figure 5) has an error of less than 3 % when compared to oil film measurements of Österlund (1999) and the George & Castillo theory. Furthermore, the smooth surface result from Hancock & Bradshaw (1989) matches with the current smooth surface data.

With the addition of roughness, the skin friction coefficient increases up to 40 %. For the rough surface measurements, probe resolution issues limited the accuracy when computing the mean velocity gradient very close to the wall. Thus, for these four cases, the expected error is estimated to be approximately 6 %. These values for Brzek *et al.* (2007) and the present investigation are in the transitionally rough regime, thus, show a considerable Reynolds number dependence. This is due to the fact that the wall shear stress is made up of both form drag and viscous stress, (i.e. $C_f = C_f(\delta^+, k^+)$). However, for the higher Reynolds number cases of the current investigation, considerably less Reynolds number dependence is visible as form drag on the surface dominates over viscous contributions.

When high free-stream turbulence is present, an increase in c_f is observed, consistent with the observations of Hancock & Bradshaw (1983) and Blair (1983). For location $L1$ ($Tu_\infty = 6.2\,\%$, $L_\infty/\delta_{99} = 0.97$) and location $L2$ ($Tu_\infty = 5.2\,\%$, $L_\infty/\delta_{99} = 0.87$), the resulting increase in c_f is 24.5 % and 15.6 %, respectively. According to Stefes & Fernholz (2004), this is due to the increased velocity gradient at the wall, as the profiles become fuller with increasing free-stream turbulence intensity. For smooth surfaces any increase in c_f must be manifested as an increased velocity gradient at the wall. However, for the rough surface measurements of the present investigation, the increased c_f can also be linked to an increase in form drag (Leonardi *et al.* 2003). Notice the smooth surface profile with high free-stream turbulence from Hancock & Bradshaw (1989) ($Tu_\infty = 4.1\,\%$, $L_e/\delta = 1.9$, $Re_\theta = 4320$) is compared with the smooth wall data with laminar free stream. Similar to the behaviour of the rough surfaces, the skin friction shows an increase due to free-stream turbulence, in this case 14 %.

With the known integral scale and turbulence intensity in the free stream, the correlation of Hancock & Bradshaw (1983) can be used as defined in the introduction at a fixed value of Re_θ. For this analysis, the value of c_{fo} used to solve for c_f from the predicted $\Delta c_f/c_{fo}$ was the rough surface skin-friction coefficient without free-stream turbulence. Note that linear interpolation and extrapolation of the rough data was used to determine C_{fo} at the required values of Reynolds numbers. Given the small Reynolds number variation where the interpolation and extrapolation is being performed, the value of C_{fo} can be approximated within several percent of its true value. The resulting predicted values agree with the measured values within 3 %, within the uncertainty of the measured values from (3.1).
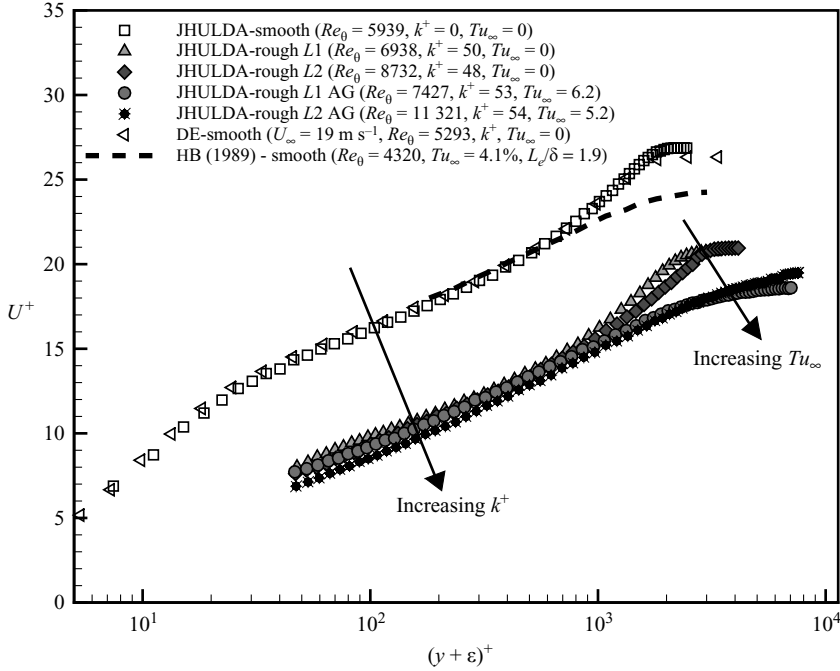
FIGURE 6. Mean velocity profiles in inner variables, and a comparison with a standard prior result (DeGraaff & Eaton 2000) for smooth wall without free-stream turbulence at similar Reynolds number (open triangles).

4. Profiles in inner variables

4.1. *Mean velocity*

To begin the analysis of the velocity field, the mean velocity profiles are plotted in figure 6 in inner coordinates to observe the effects of roughness and free-stream turbulence intensity. The smooth surface measurement is compared with the data of DeGraaff & Eaton (2000), as well as the smooth surface data with high free-stream turbulence of Hancock & Bradshaw (1989). The smooth surface profile of the present investigation matches with the profile of DeGraaff & Eaton (2000). When comparing the data of the present investigation with that of Hancock & Bradshaw (1989), it is clear that free-stream turbulence has a significant impact on the outer region and more pronounced in the wake region. As described in Hancock & Bradshaw (1983), Blair (1983) and Stefes & Fernholz (2004), a significant decrease in the wake region is seen for increasing free-stream turbulence. For example, Hancock & Bradshaw (1989) stated that since $(U_\infty - U)/u_\tau$ depends on both Tu_∞ and L_∞/δ, a wake function with a single wake strength argument is inadequate.

When the four rough surface profiles are considered, several known behaviours are observed. As is well known, the downward shift in the profiles for rough surfaces (i.e. roughness function) relates directly to the roughness parameter k^+. For this sand grain type roughness, the larger the roughness parameter, the larger the downward shift. It is important to note that for the two cases with high free-stream turbulence, the friction velocity increases, and thus the effective roughness parameter also increases. Furthermore, similar to the smooth surface profile with high free-stream turbulence, the rough profiles with free-stream turbulence show a dramatically reduced wake region as well. In addition, between locations $L1$ and $L2$, the free-stream turbulence
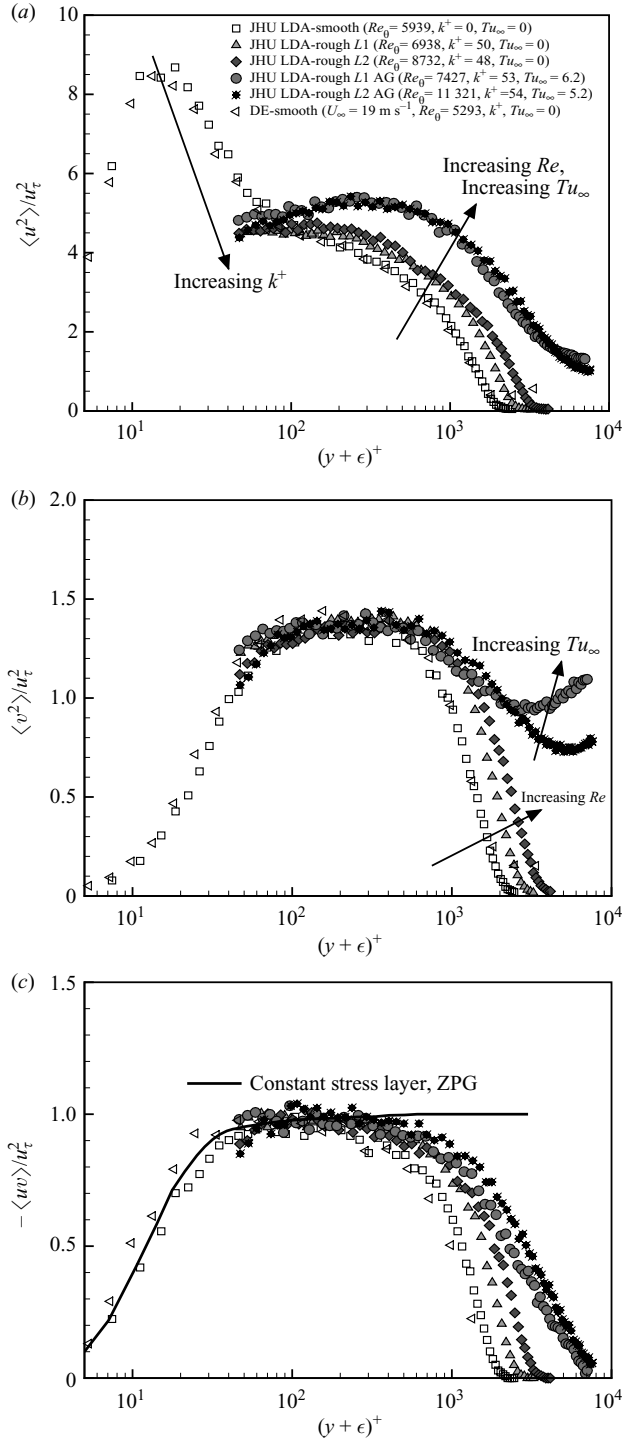
FIGURE 7. Reynolds stress profiles in inner units for the various measurement cases, and a comparison with a prior results (Degraaff & Eaton 2000) for smooth wall without free-stream turbulence at similar Reynolds number (open triangles). In (*c*) the solid line shows $1 - \nu dU/dy/u_\tau^2$, obtained from the data of Castillo & Johansson (2002).

decays and the wake region begins to increase. The behaviour of the wake parameter Π is also observed in table 3.

4.2. *Reynolds stresses*

The Reynolds stress profiles are shown in figures 7 in inner variables. The smooth surface profiles are also compared to the data of DeGraaff & Eaton (2000) at a similar Reynolds number. Figure 7(*a*) shows the streamwise fluctuations, $\langle u^2 \rangle$ versus $(y+\epsilon)^+$. As demonstrated in many investigations (Ligrani & Moffat 1986; Jiménez 2004, etc.), roughness destroys the high peak near the wall due to the breakdown of the viscous region. This appears to be the case in the present data, both with and without free-stream turbulence. The free-stream turbulence increases the magnitude of the streamwise fluctuations significantly for all wall distances greater than $(y+\epsilon)^+ > 100$, that is to say over most of the boundary layer due to the addition of inactive motions. Only for wall distances $(y+\epsilon)^+ < 100$ does the free-stream turbulence not appreciably increase the profiles. At the edge of the boundary layer, the $\langle u^2 \rangle$ profiles do not go to zero for the cases with high free-stream turbulence but converge to the free-stream values. As expected, turbulence decay occurs with downstream evolution of the free stream (Comte-Bellot & Corrsin 1966). For the cases without free-stream turbulence, in the outer layer the expected outward shifting with increasing Reynolds number is apparent.

For the wall-normal fluctuations $\langle v^2 \rangle$ shown in figure 7(*b*), there is little effect of roughness on the $\langle v^2 \rangle$ profiles in inner variables when the Reynolds number is similar. Also notice that below $(y+\epsilon)^+ < 1000$, the profiles with high free-stream turbulence do not show an increase, contrary to the streamwise Reynolds stress component. This clearly indicates the importance of the wall boundary condition imposed on the wall-normal Reynolds stress profiles due to the pressure field. This influence is felt far away from the wall (for $(y+\epsilon)^+ < 1000$ in this case) and acts to dampen the wall-normal fluctuations despite the free-stream turbulence. This constraint does not exist for the streamwise Reynolds stress. Notice the high magnitude of the wall-normal fluctuations due to the AG in the outer region, as well as the decay between locations *L1* and *L2*. Aronson *et al.* (1996) showed damping in shear free turbulence as far as two integral scales from the wall, which in this case is significantly larger than the boundary layer thickness.

Similarly, the Reynolds shear stress, $-\langle uv \rangle$ in figure 7(*c*) does not show differences between the smooth, rough and rough with free-stream turbulence in the inner layer, and no Reynolds number dependence exists there. Thus, it appears that the active motions ($\langle v^2 \rangle$ and $-\langle uv \rangle$) are less affected by the free-stream turbulence in the logarithmic region than the inactive motion ($\langle u^2 \rangle$). This has a significant effect on the correlation coefficient as well, although roughness did not have an effect on this parameter. The Reynolds number is high enough for all cases, with the possible exception of the smooth surface profile, for a constant stress layer to form (i.e. $-\langle uv \rangle / u_\tau^2 \approx 1$ for $30 < (y+\epsilon)^+ < 0.1\delta^+$). The solid line in figure 7(*c*) shows the behaviour of (3.1) from the smooth wall data of Castillo & Johansson (2002) which represents $1 - \nu dU/dy/u_\tau^2$. As expected the profiles show a Reynolds number dependence in the outer layer. Also, there is a non-negligible contribution of $-\langle uv \rangle$ of 5 % at $(y+\epsilon)^+ > \delta^+$. This indicates that this term still contributes to the momentum equation in the free-stream boundary layer interface. Given the experimental limitations, measurements could not be made farther into the free stream to determine if the Reynolds shear stress reaches a value of zero. Although convergence in the mean velocity was reached, possible (outer) intermittency may still contribute to a slight Reynolds stress contribution in this region.

5. Profiles in outer variables

5.1. *Mean velocity*

To illustrate the effects of roughness and free-stream turbulence on the outer flow, the mean velocity deficit profiles are shown in figure 8. The mean deficit profiles are normalized by two scaling techniques: the classical scaling u_τ and the Zagarola & Smits (1998) scaling $U_\infty \delta^*/\delta$. These data in outer variables are again compared with the smooth surface data of DeGraaff & Eaton (2000) (smooth) and Hancock & Bradshaw (1989) (smooth w/free-stream turbulence) at a similar Reynolds number.

As shown in many investigations (Castro 2007; Schultz & Flack 2007), when the Reynolds number is relatively high and the ratio of $k/\delta < 0.02$, the friction velocity scale in effect absorbs the effects of roughness on the velocity deficit profiles in ZPG flows only, Cal *et al.* (2008). As is evident in figure 8(*a*), this is also the case from the present results, within the uncertainty associated with computing u_τ. However, when high free-stream turbulence is present, the shape of the velocity deficit profiles is completely different than the smooth or rough surface profiles. This is also true for the data of Hancock & Bradshaw (1989). The profiles become fuller, indicating that higher momentum flux towards the wall exists. Also notice that the rough profiles with high free-stream turbulence collapse with the smooth profile with high free-stream turbulence. This further confirms that the friction velocity is very good at removing the effects of roughness. The behaviour observed with the rough profiles with high free-stream turbulence is consistent with the results of Thole & Bogard (1996) with free-stream turbulence intensity $Tu_\infty > 10\%$ at a lower Reynolds number. In the present case, no difference is observed between the profiles at the two downstream locations (i.e. free-stream turbulence decay from 6.2% to 5.2%).

Figure 8(*b*) shows that when the Zagarola & Smits (1998) scaling $U_\infty \delta^*/\delta$ is used, the smooth and rough surface profiles without free-stream turbulence collapse to a single curve. This scaling was shown to successfully remove the effects of roughness, upstream conditions and Reynolds number from the outer flow in Seo *et al.* (2004). In fact the collapse appears to be slightly better than with the u_τ scaling used in figure 8(*a*), although the differences are within the experimental uncertainty. When considering the case with free-stream turbulence, the curves with Zagarola & Smits (1998) scaling are closer to those without free-stream turbulence. However, their shape is qualitatively still different. This underscores the inability of the friction velocity or the Zagarola & Smits (1998) scalings to absorb the effects of free-stream turbulence for either smooth or rough surfaces. Certainly, the structure of these profiles is very different in the outer layer. It appears unlikely that a single or single additional scale (length or velocity) could collapse all profiles with free-stream turbulence.

5.2. *Boundary layer parameters*

Boundary layer parameters were also investigated with a focus on the effect of high free-stream turbulence on the turbulent boundary layer. These parameters are compared to the results of Castillo & Johansson (2002) and Brzek *et al.* (2007), which were obtained at similar experimental conditions to the present investigation.

Figure 9(*a*) shows the ratio of displacement thickness to boundary layer thickness δ^*/δ_{95}. Roughness significantly increases this parameter when compared to smooth surfaces. Over the range of Reynolds numbers, the smooth surface values of Castillo & Johansson (2002) and the present investigation are relatively constant. The similarity theory of George & Castillo (1997) predicts that δ^*/δ approaches a constant in the limit of infinite Reynolds number for smooth surfaces. The rough surface measurements without free-stream turbulence of the present investigation are also shown as upward triangles and diamonds. Over the Reynolds number range,
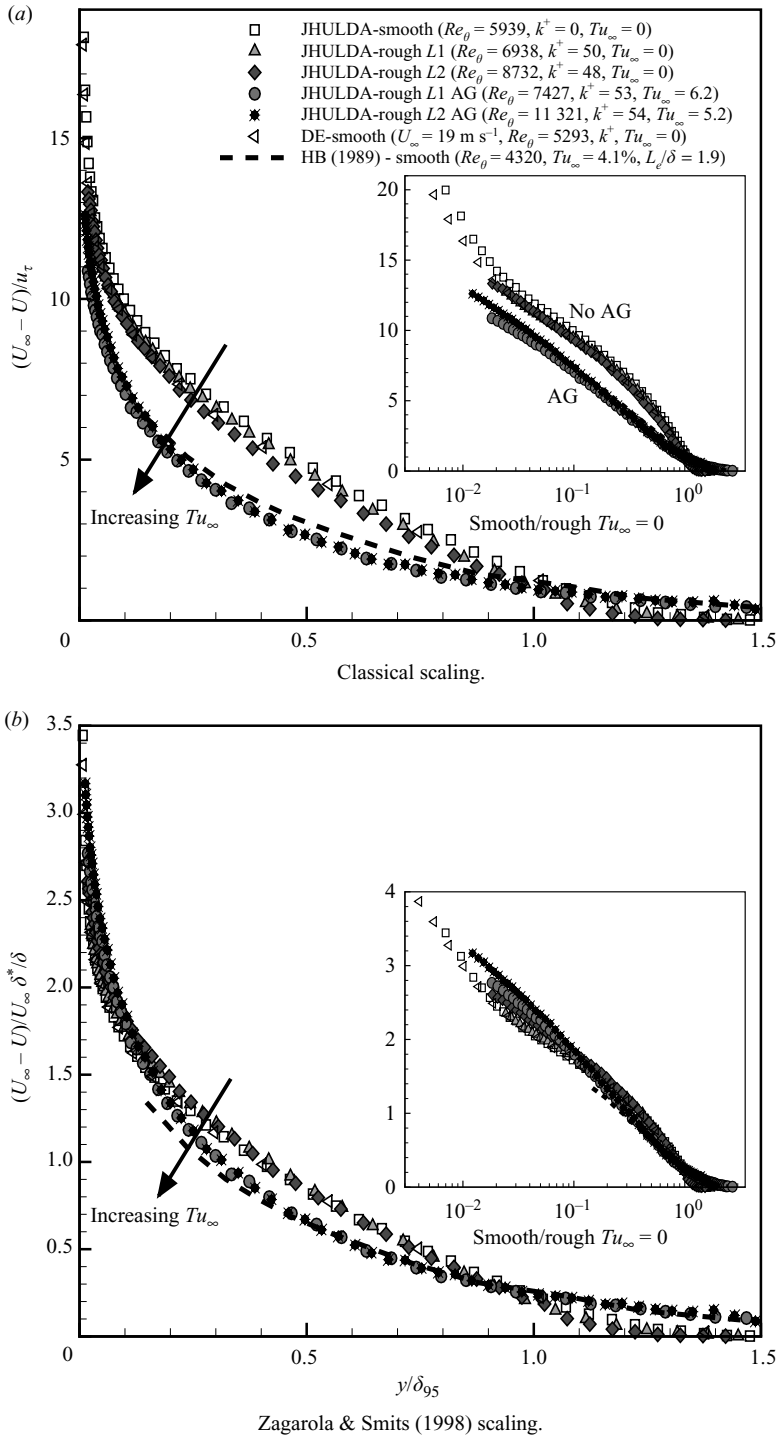
(*a*)

Classical scaling.

(*b*)

y/δ_{95}

Zagarola & Smits (1998) scaling.

FIGURE 8. Mean velocity deficit profiles using outer scaling, for smooth and rough surfaces.

(i.e. $3400 < Re_\theta < 9300$), the values of δ^*/δ_{95} for rough surfaces without free-stream turbulence decrease monotonically. This is consistent with the Zagarola & Smits (1998) scaling for the velocity deficit profiles which collapses smooth and rough surface profiles onto a single curve.
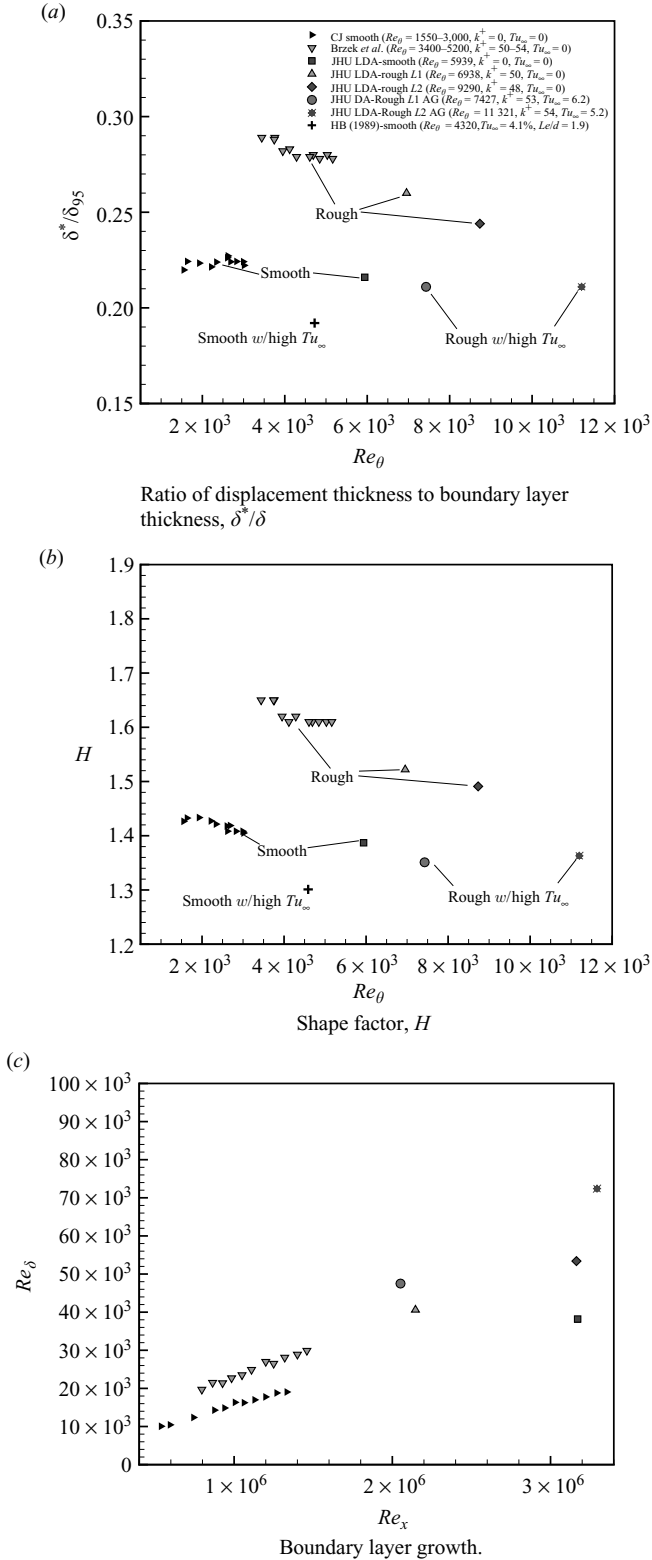
FIGURE 9. Evolution of boundary layer parameters.

When the high free-stream turbulence intensity is present, δ^*/δ_{95} shows a significant reduction as observed with the data of Hancock & Bradshaw (1989). For the rough surface profiles with high free-stream turbulence, the values of δ^*/δ_{95} show a dramatic reduction, even to values lower than the smooth surface case, and do not show any change with Reynolds number. The decrease in δ^*/δ_{95} indicates that the amount of entrainment into the boundary layer significantly increases when compared to the increase in boundary layer thickness. This is confirmed by the velocity profiles which have much higher velocities closer to the wall. Also, as noted in George (1990), this increased entrainment is due to the importance of the free-stream wall-normal fluctuations as it relates to the y-momentum equation. Specifically, George (1990) notes that a highly turbulent free-stream alters the wall-normal pressure field and increases the entrainment in the boundary layer.

The shape factor $H = \delta^*/\theta$ is shown in figure 9(b) and comparisons can be made for smooth with and without free-stream turbulence, and rough with and without free-stream turbulence. Observations are in general quite similar to those made for δ^*/δ. Among others, when high free-stream turbulence is present, a significant reduction of H is seen, with the rough data points decreasing below the smooth surface values. This implies that even with the increase in mixing, the price is a relatively larger increase in drag.

The dynamic importance of these two boundary layer parameters, as well as the increase in skin friction, is significant. With high free-stream turbulence, a fuller velocity profile exists, which represents higher momentum flux closer to the wall and thus the possibility to prevent separation in the presence of adverse pressure gradient (APG). For instance, this was shown in the investigation of Kalter & Fernholz (2001), where an APG flow with high free-stream turbulence was studied. Measurements near and downstream of a separation bubble were shown to be highly affected by the free-stream turbulence. The size of the separated region decreases drastically for the cases presented, and in fact, was eliminated all together for the highest free-stream turbulence level.

Figure 9(c) shows the boundary layer growth for the three different sets of conditions: (i) smooth, (ii) rough and (iii) rough with free-stream turbulence. Clearly, roughness increases the boundary layer growth, when compared to the smooth surface, seen here over a significant Reynolds number range. When high free-stream turbulence is present, the boundary layer growth further increases due to the increased mixing between the boundary layer and free-stream turbulence. This leads to an increase of nearly 26 % in the boundary layer thickness at $Re_x = 3.2 \times 10^6$, when compared to the corresponding rough surface with laminar free stream.

5.3. *Reynolds stresses*

The Reynolds stresses are plotted in figure 10 as a function of y/δ_{95} to emphasize the effects of roughness and free-stream turbulence on the outer region. Figure 10(a) shows the streamwise Reynolds stress component normalized with u_τ^2. Clearly this scaling is able to remove the effects of roughness from the outer flow ($y/\delta_{95} > 0.1$), where both the smooth and rough profiles collapse. However, the increase of $\langle u^2 \rangle$ due to free-stream turbulence exists throughout the entire layer, all the way down to $y/\delta_{95} \sim 0.07$. For instance, at $y/\delta_{95} = 0.2$, there is a 25 % increase in the streamwise fluctuations, 40 % increase at $y/\delta_{95} = 0.6$ and 54 % at $y/\delta_{95} = 1.0$. In absolute terms, the increase appears nearly uniform, comparable to the magnitude of the free-stream turbulence. The decay of the streamwise fluctuations can be seen between locations $L1$ and $L2$, and is significant throughout the entire boundary layer and not just in the free stream.
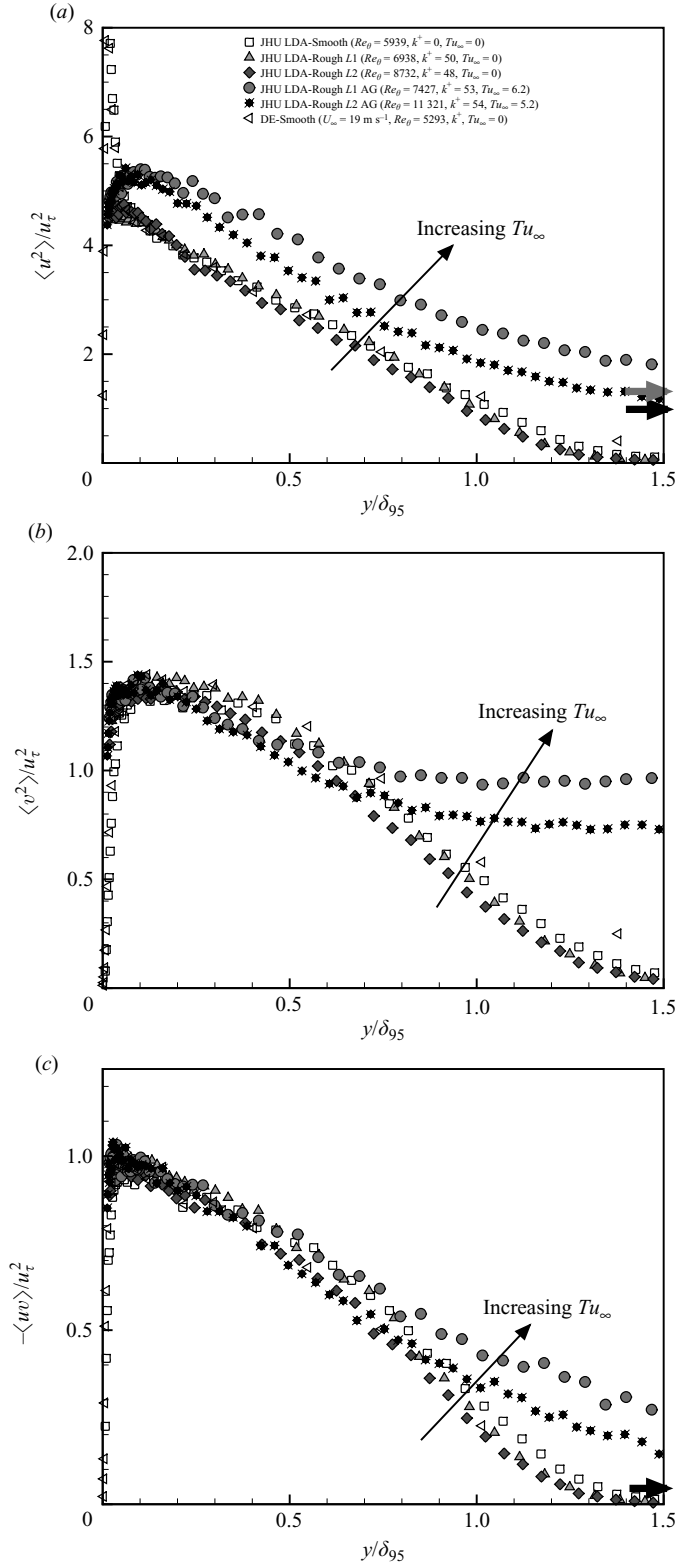
FIGURE 10. Reynolds stress profiles as function of y/δ_{95}.

Such a uniform increase in the $\langle u^2 \rangle$ profiles creates the appearance of the sum of two separate profiles: the $\langle u^2 \rangle$ profile without free-stream turbulence added to a constant value equal to the free-stream turbulence level. It is useful to recall that the variance of a process consisting of the sum of two uncorrelated processes is the sum of the component variances. Thus the measured $\langle u^2 \rangle$ profiles suggest that the streamwise fluctuations of the boundary layer and free-stream turbulence behave as almost uncorrelated processes. Of course, this does not mean that the two processes are statistically independent. Also, the superposition holds neither exactly nor uniformly. For instance, one notes that the magnitude of $\langle u^2 \rangle$ in the free stream for y/δ_{95} between 1.2 and 1.5 still significantly exceeds the asymptotic state of the $\langle u^2 \rangle$ profiles, shown by the two horizontal arrows.

The wall-normal Reynolds stress profiles in figure 10(b) show that for the sand grain roughness in the present investigation, the classical scaling is able to absorb the effects of roughness throughout the entire boundary layer, and the effects of the high free-stream turbulence all the way up to $y/\delta_{95} < 0.7$. Thus, the wall-normal Reynolds stresses behave very differently from the streamwise Reynolds stresses in the region between $0.07 < y/\delta_{95} < 0.7$. Unlike for the streamwise component, the variance contributions of the free-stream turbulence and boundary layer are not additive. Instead, the $\langle v^2 \rangle$ profiles appear to select the largest of the two contributions. Returning to the interpretation of the profile as resulting from the sum of two processes, the observed behaviour suggests that there is strong (anti) correlation among them in the range $0.07 < y/\delta_{95} < 0.7$. Dynamically, such anticorrelation may be mediated by non-local pressure fluctuations across the boundary layer due to the wall blocking effect.

Similar to the $\langle v^2 \rangle$ component, the Reynolds shear stress $-\langle uv \rangle$ does not show the effects of roughness when using the classical scaling in figure 10(c). Furthermore, only in the outer layer $y/\delta_{95} > 0.8$ is the effect of free-stream turbulence visible. Notice the significant contribution of $-\langle uv \rangle$ at $y/\delta_{95} = 1.5$, indicating the effectiveness of free-stream turbulence in diffusing the boundary layer including its momentum transport effects. For both profiles at the last measurement position ($y/\delta_{95} > 2.0$), the value of $-\langle uv \rangle/u_\tau^2$ is still 5 %, as shown by the arrow in figure 10(c).

As a result of the differing effects on streamwise and wall-normal Reynolds stresses, the addition of isotropic turbulence in the free stream has the effect of increasing turbulence anisotropy over much of the boundary layer, between $y/\delta_{95} \sim 0.07$ and $y/\delta_{95} \sim 0.7$. An important question is what turbulence length scales contribute mostly to such an increase in anisotropy. This is addressed in the next section using second-order structure functions.

5.4. *Second-order structure function*

The second-order structure functions (Monin & Yaglom, 1971) for velocity components u or v are defined according to

$$\langle \delta_r u^2 \rangle \equiv \langle (u(x+r) - u(x))^2 \rangle, \qquad \langle \delta_r v^2 \rangle \equiv \langle (v(x+r) - v(x))^2 \rangle. \qquad (5.1)$$

The spatial separation r is specified using Taylor's frozen hypothesis from $r = U\Delta t$ to convert time into spatial separation. Given the uneven time intervals of the LDA sampling, particular care must be applied when evaluating the structure functions. Specifically, the range of scales r considered is divided into twenty five separate 'bins' and logarithmically spaced between 7 and 900 mm. The limits of this interval are picked based on the average data rate of the LDA samples, as well as the estimated length scales in the flow. If the separation of consecutive data points falls within one of these 'bins' it is counted towards the evaluation of the average structure function
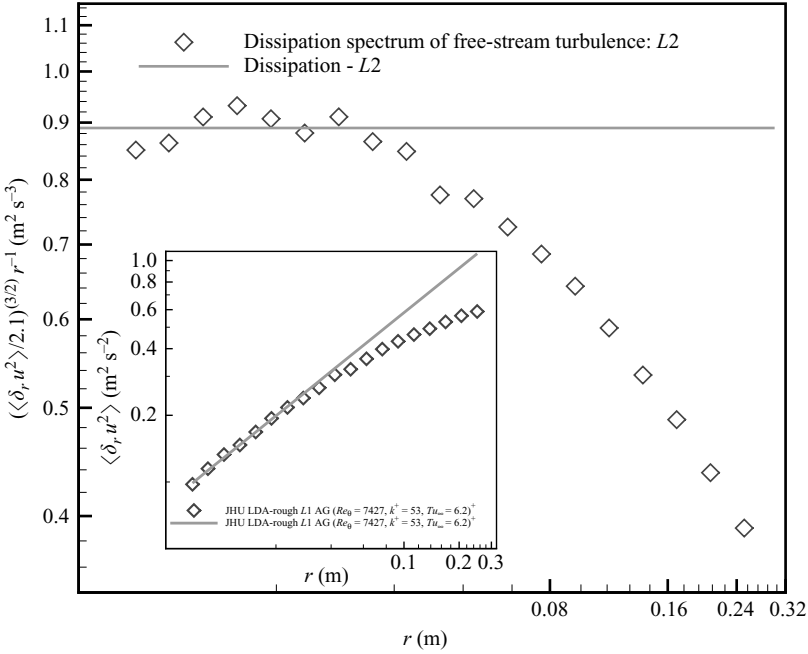
FIGURE 11. Premultiplied structure function $\varepsilon(r) = (\langle\delta_r u^2\rangle/2.1)^{3/2}r^{-1}$ versus displacement r. The horizontal line displays the inferred dissipation rate. The insert shows the non-premultiplied second-order structure function together with $2.1\varepsilon^{2/3}r^{2/3}$ using the value of $\varepsilon = 0.89\,\mathrm{m^2\,s^{-3}}$ measured in the main figure.

at the particular mid-point bin value of r. In the section below (§5.4.1), this approach is used to evaluate the dissipation in the free-stream turbulence (that was used in §2 to estimate the integral scale of the free-stream turbulence). In §5.4.2, the measured structure functions are used to quantify the contributions to the Reynolds stress profiles and anisotropy in the boundary layer.

5.4.1. *Calculation of the dissipation using the second-order structure function*

To estimate the dissipation in the nearly isotropic free stream, the classic Kolmogorov scaling of the second-order structure function approach is used (Monin & Yaglom 1971). This scaling is valid in the inertial range $\eta_{k_\infty} \ll r \ll L_\infty$, where η_{k_∞} is the Kolmogorov length scale, r is the displacement length and L_∞ is the integral length scale. For the streamwise velocity component, the Kolmogorov scaling is given by

$$\langle\delta_r u^2\rangle \approx C_2 \epsilon^{2/3} r^{2/3}, \qquad (5.2)$$

with $C_2 \approx 2.1$, the empirically well-known Kolmogorov constant.

Figure 11 shows the premultiplied quantity, $\varepsilon(r) = (\langle\delta_r u^2\rangle/2.1)^{3/2}r^{-1}$ for location $L2$ in the free stream. The dissipation needed in (2.1) is estimated from this distribution when $\varepsilon(r)$ is approximately constant across the inertial range. The value $\varepsilon = 0.89\,\mathrm{m^2\,s^{-3}}$ is shown by the solid line in figure 11. For location $L1$ the value measured in similar fashion is $\varepsilon = 1.46\,\mathrm{m^2\,s^{-3}}$.

Furthermore, the dissipation in the free stream could be estimated based on the advection–dissipation balance in the equation for decaying kinetic energy $\epsilon = -U_\infty \mathrm{d}k/\mathrm{d}x$. A power-law decay is assumed $k(x) = Cx^{-n}$. Using measured values for k at $L1$ and $L2$ allows us to evaluate C for both locations. The distance between the plate leading edge and the AG is 1.05 m. At $L1$ ($x = 3.15 + 1.05\,\mathrm{m}$) we have $k = 0.5\,\mathrm{m^2\,s^{-2}}$, and at $L2$ ($x = 4.76 + 1.05\,\mathrm{m}$) we have $k = 0.38\,\mathrm{m^2\,s^{-2}}$. Therefore

$C = 3.0 \, \text{m}^{3.25} \, \text{s}^{-2}$ at $L1$ and $C = 3.45 \, \text{m}^{3.25} \, \text{s}^{-2}$ at $L2$. Using the decay exponent $n = 1.25$ measured in Kang *et al.* (2003), and the slightly different values of U_∞ in both cases (see table 2) allows us to evaluate the dissipation from $\epsilon = -U_\infty \mathrm{d}k/\mathrm{d}x = U_\infty C n x^{-n-1}$. We obtain $\epsilon = 1.46 \, \text{m}^2 \, \text{s}^{-3}$ at $L1$ and $\epsilon = 0.85 \, \text{m}^2 \, \text{s}^{-3}$ at $L2$, i.e. differences of less than 1 % for $L1$ and 4 % at location $L2$. This is excellent agreement considering the various assumptions involved in the two methods of evaluating the dissipation.

Using the measured value for the dissipation, the inertial-range scaling of the second-order structure function can be verified by comparing the structure function plotted as a function of r with the right-hand side of (5.2) for location $L1$. This appears in the insert in figure 11 and good agreement exists in the inertial range.

5.4.2. *Contributions of various scales to anisotropy in the boundary layer*

The structure functions can be interpreted as (twice) the energy content and contribution to the velocity variances (Reynolds stresses) of scales up to the separation r considered. In the limit $r \to \infty$, when two-point correlations decay to zero, the structure function coincides with twice the variance. Figure 12 shows the structure function plotted against r/y, at several values of y/δ_{95}. The values of y/δ_{95} were selected to be as close as possible for the cases with and without free-stream turbulence, and considering only the data points with sufficiently high data rates.

Different behaviours are seen at increasing distances from the wall. Figure 12(*a*) shows that closer to the wall (for $y/\delta_{95} \sim 0.1$), there is good agreement between the cases with and without free-stream turbulence, up to scales of 300 mm. However, significant differences between the streamwise and wall-normal structure functions exist. Most of the data shown are for displacements $r > y$, thus the data in this plot correspond to turbulence length scales that are larger than the local turbulence 'large scales'. Hence, the presence of significant anisotropy is consistent with expectations.

When considering data at larger distances from the wall, near the middle of the boundary layer in outer units ($y/\delta_{95} \sim 0.6$), results shown in figure 12(*b*) are obtained. It shows that for displacements up to $r/y \leqslant 0.4$ the streamwise and wall-normal structure functions are of similar order of magnitude. This is consistent with isotropy of the small-scale structure of turbulence. At larger displacements, both with and without free-stream turbulence, an increasing difference is seen between the streamwise and wall-normal structure functions. Moreover, it is noticeable that up to $r/y \sim 3$ the streamwise structure functions for the case with and without free-stream turbulence show similar values. In contrast, the wall-normal structure functions for cases with and without free-stream turbulence show some disagreement for displacements greater than $r/y \sim 0.6$.

In the free stream (above $y/\delta_{95} \sim 1.1$), different behaviours are seen depending on the levels of free-stream turbulence in the flow. From figure 12(*c*), it is seen that with higher free-stream turbulence, the structure functions are of comparable magnitude (i.e. more isotropic) for $r/y \leqslant 0.5$. On the contrary, at larger length scales, the results indicate increasing anisotropy.

To better ascertain the impact of these trends on the Reynolds stress distributions discussed earlier, in figure 13 the structure functions are shown at fixed displacements r/δ_{95} as a function of distance to the wall. Three different fixed displacements are considered: $r = 7 \, \text{mm}$ (corresponding to $r/\delta_{95} = 0.087$ for the case without AG and $r/\delta_{95} = 0.067$ with AG), $r = 250.9 \, \text{mm}$ ($r/\delta_{95} = 3.13$ without AG, $r/\delta_{95} = 2.40$ with AG) and $r = 827.4 \, \text{mm}$ ($r/\delta_{95} = 10.31$ without AG and $r/\delta_{95} = 7.91$ with AG). Figure 13(*a*) shows the smallest length scale examined and it is seen that, for both levels of free-stream turbulence, the values for the streamwise and wall-normal structure functions are almost the same for all values of y/δ_{95}. Turbulence variance at small scales is
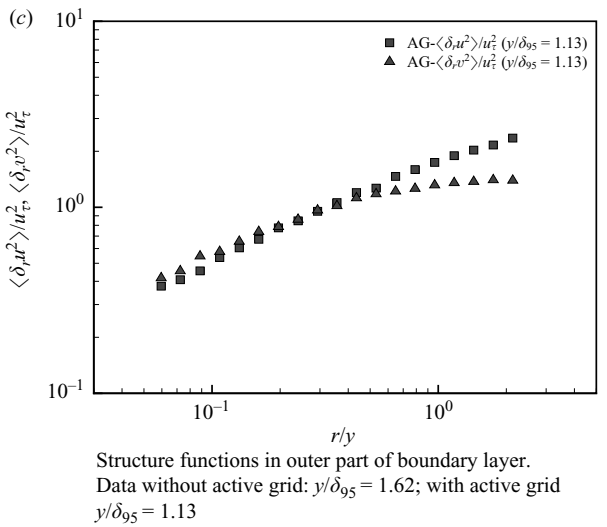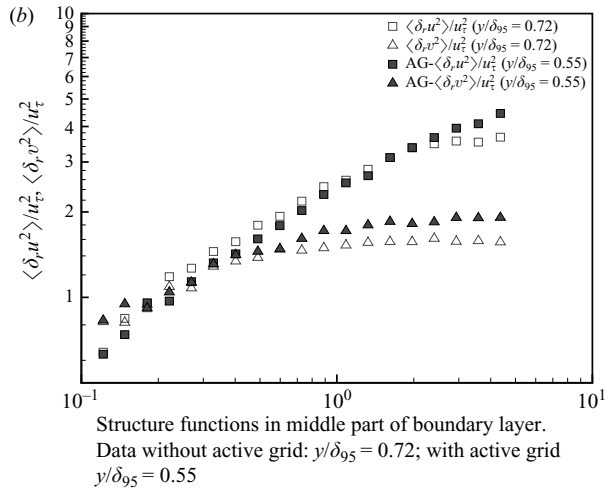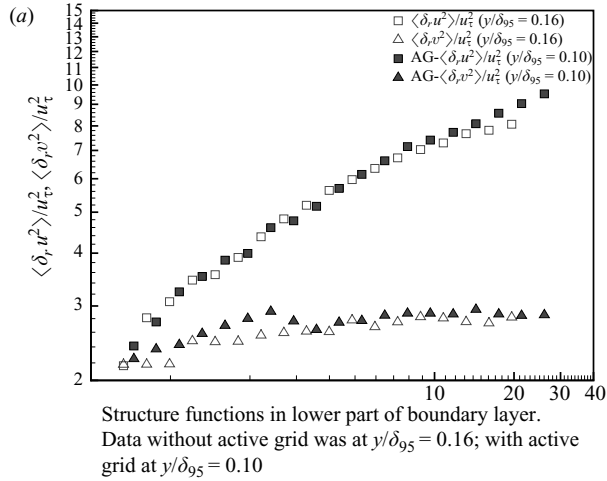
(*a*) Structure functions in lower part of boundary layer. Data without active grid was at $y/\delta_{95} = 0.16$; with active grid at $y/\delta_{95} = 0.10$

(*b*) Structure functions in middle part of boundary layer. Data without active grid: $y/\delta_{95} = 0.72$; with active grid $y/\delta_{95} = 0.55$

(*c*) Structure functions in outer part of boundary layer. Data without active grid: $y/\delta_{95} = 1.62$; with active grid $y/\delta_{95} = 1.13$

FIGURE 12. Stream-wise and wall-normal second-order structure functions versus r in three different y/δ_{95} regions.

(a) Structure functions at $r/\delta_{95} = 0.087$ for the data without active grid and $r/\delta_{95} = 0.067$ with the active grid ($r = 7$ mm)

(b) Structure functions at $r/\delta_{95} = 3.13$ for the data without active grid and $r/\delta_{95} = 2.40$ with active grid ($r = 250.9$ mm)

(c) Structure functions at $r/\delta_{95} = 10.31$ for the data without active grid and $r/\delta_{95} = 7.91$ with active grid ($r = 827.4$ mm)
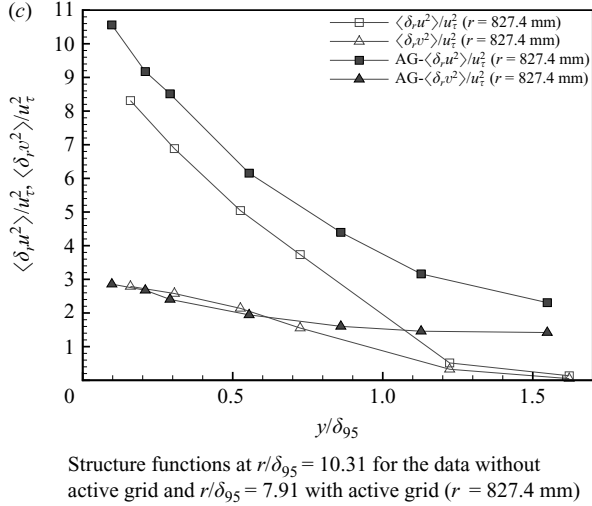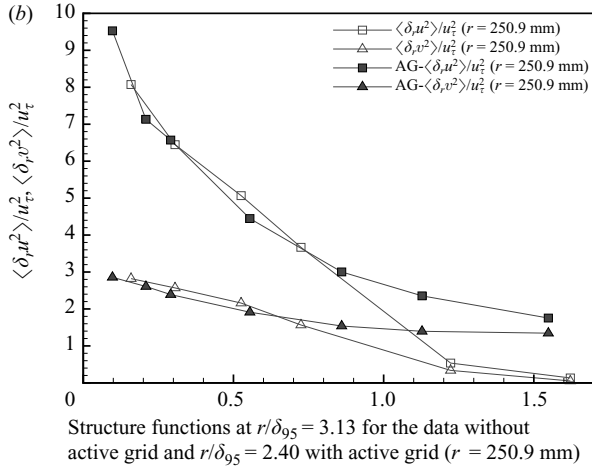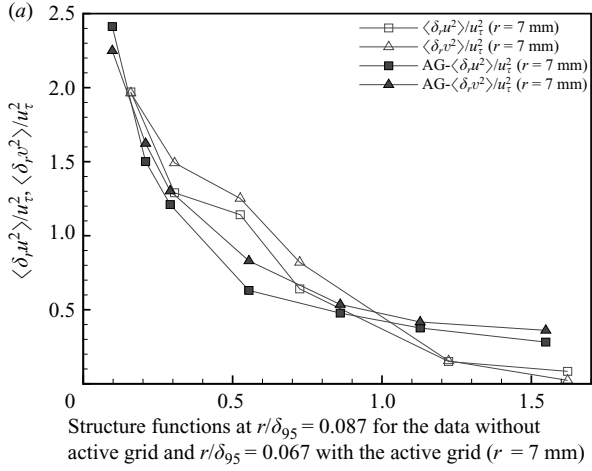
FIGURE 13. Second-order structure function versus y/δ_{95} at fixed values of r.

therefore nearly isotropic both with and without free-stream turbulence. As expected for heights above the boundary layer thickness, the structure functions without free-stream turbulence tend to very small values (but not exactly equal to zero due to non-turbulent irrotational fluctuations), whereas those with free-stream turbulence tend to the non-zero values in the free stream.

The case of an intermediate length scale of $r = 250.9$ mm ($r/\delta_{95} = 3.13$ without the AG and $r/\delta_{95} = 2.40$ with AG) is shown in figure 13(b). At these large scales a significant difference between the streamwise and the wall-normal structure functions exists, indicating anisotropy. This is consistent with the view that the scale $r = 250.9$ mm is above the local turbulence 'large scale' at heights below $y/\delta_{95} \sim 1.2$. As before, for $y/\delta_{95} > 1$, the structure functions without streamwise turbulence tend to zero. Most notable in this figure, however, is the fact that unlike the Reynolds stresses, the profiles with and without AG still collapse.

For the largest separation considered, $r = 827.4$ mm ($r/\delta_{95} = 10.31$ without AG, $r/\delta_{95} = 7.91$ with AG), shown in figure 13(c), one now notices a significant difference between the structure functions for the streamwise component, with and without streamwise turbulence. That is to say, in comparing figures 13(b) and 13(c), we may conclude that the anisotropy arises from scales below 827 mm, and above 251 mm. The addition of isotropic turbulence in the free stream increased the anisotropy when interacting with the boundary layer, and this occurs via very large structures, causing correlations in the streamwise direction at scales between 3 and 10 times the boundary layer thickness. Moreover, notice that for the streamwise structure function, differences exist throughout the entire boundary layer, consistent with the streamwise Reynolds stress profiles (see figure 10a). However, no difference is seen in the wall-normal structure function below $y/\delta_{95} = 0.6$. Now, for $y/\delta_{95} > 0.6$, there are differences in the structure functions, with and without free-stream turbulence. Notice that these observations in the structure function are consistent with the behaviour of the wall-normal Reynolds stresses (see figure 10b).

Figure 14 shows the two-point correlation functions of u and v. For the cases without free-stream turbulence, the streamwise correlation functions decay to almost zero before $r/\delta_{95} \approx 3$. On the other hand, for the case with free-stream turbulence, the streamwise correlation function reaches small values only at $r/\delta_{95} \approx 8$. In contrast, the wall-normal correlation function, for the case with free-stream turbulence, reaches small values at $r/\delta_{95} \approx 3$ and approximately $r/\delta_{95} \approx 1$ without free-stream turbulence. This suggests that the free-stream turbulence near the boundary layer contains very elongated structures in the streamwise direction, with streamwise coherency in the streamwise velocity, but far less coherency in the wall-normal velocity component. Moreover, notice that the difference between the streamwise and wall-normal correlation functions for the cases with and without free-stream turbulence are consistent with the behaviour of the streamwise and wall-normal Reynolds stresses when under the appropriate free-stream conditions.

6. Reynolds stress equations

This section examines some of the terms in the Reynolds stress equations to shed light on the effects of free-stream turbulence on production and turbulence diffusion. The Reynolds stress equations are written for the outer region, neglecting the viscous turbulence transport term, the $\partial U/\partial x$, $\partial V/\partial x$ and $\partial V/\partial y$ terms in the turbulence production, and the streamwise gradient terms $\partial/\partial x$ in the turbulent transport. The equations are listed below.
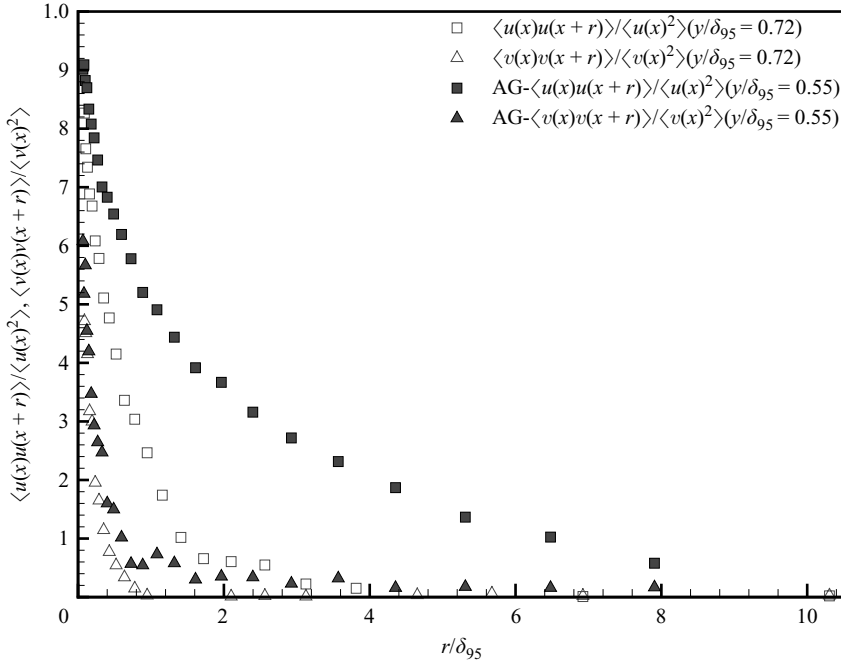
FIGURE 14. Two-point correlation functions of u and v versus r/δ_{95}, at a fixed height, at $y/\delta_{95} = 0.72$ (without AG) and $y/\delta_{95} = 0.55$ (with AG).

Stream-wise velocity variance (negative Reynolds stress) equation:

$$\left[U\frac{\partial\langle u^2\rangle}{\partial x} + V\frac{\partial\langle u^2\rangle}{\partial y} \right] = \left\langle \frac{p}{\rho}\left[2\frac{\partial u}{\partial x} \right] \right\rangle + \frac{\partial}{\partial y}[-\langle u^2 v\rangle] - 2\langle uv\rangle\frac{\partial U}{\partial y} - 2\epsilon_{uu}. \qquad (6.1)$$

Reynolds shear stress equation:

$$U\frac{\partial\langle -uv\rangle}{\partial x} + V\frac{\partial\langle -uv\rangle}{\partial y} = \left\langle \frac{p}{\rho}\left[\frac{\partial v}{\partial x} + \frac{\partial u}{\partial y} \right] \right\rangle + \frac{\partial}{\partial y}[-\langle pu\rangle - \langle v^2 u\rangle] - \langle v^2\rangle\frac{\partial U}{\partial y} - \epsilon_{uv}. \qquad (6.2)$$

Wall-normal velocity variance (negative Reynolds stress) equation:

$$U\frac{\partial\langle v^2\rangle}{\partial x} + V\frac{\partial\langle v^2\rangle}{\partial y} = \left\langle \frac{p}{\rho}\left[2\frac{\partial v}{\partial y} \right] \right\rangle + \frac{\partial}{\partial y}[-2\langle pv\rangle - \langle v^3\rangle] - 2\epsilon_{vv}. \qquad (6.3)$$

The ϵ-terms are viscous dissipation terms for each component. Below, the production of Reynolds stress is examined first.

6.1. *Turbulent production*

The production of Reynolds stress is defined in general according to

$$P_{ij} = -\langle u_i u_k\rangle\frac{\partial U_j}{\partial x_k} - \langle u_j u_k\rangle\frac{\partial U_i}{\partial x_k}. \qquad (6.4)$$

In evaluating the production terms from our data, the terms involving $\partial U/\partial x$, $\partial V/\partial x$ and $\partial V/\partial y$ are neglected since they are very small compared to the term involving $\partial U/\partial y$ in (6.1) and (6.2), that is to say, $P_{11} = -2\langle uv\rangle\,\mathrm{d}U/\mathrm{d}y$, and $P_{12} = -2\langle v^2\rangle\,\mathrm{d}U/\mathrm{d}y$. It should be noted in this approximation that the wall-normal Reynolds stress

equation does not contain a production term. This will be discussed later, since there is a significant increase in the $\langle v^2 \rangle$ profiles in the outer region. To compute the gradient term $\mathrm{d}U/\mathrm{d}y$ the velocity profile is locally curve-fit using least square error to multiple regions, using polynomial forms of order 3 or 4, depending on the region of the boundary layer being fit. The regions cover approximately 20 neighbouring points, and the different regions are connected in such a way that both the function and derivative are continuous.

To isolate the effects of the free-stream turbulence on the turbulence production, the P_{11} and the $-P_{12}$ profiles are normalized with u_τ^3/δ_{95}. Results of §5.3 showed that the effects of roughness on the velocity profiles and Reynolds stresses are removed with this scaling, since the criteria set forth for the attached eddy hypothesis are achieved, (i.e. $k/\delta < 0.02$ with a sufficiently high Reynolds number). This provides the ability to focus solely on the effects of the free-stream turbulence.

The results for the production of $\langle u^2 \rangle$ in figure 15(a) confirm that with this scaling the turbulent production between smooth and rough are quite similar. However, interesting features occur in the profiles with high free-stream turbulence. It should be noted that the streamwise Reynolds stress profiles $\langle u^2 \rangle$ showed a significant increase throughout the entire boundary layer, due to the presence of high free-stream turbulence (see figure 10a). However, notice that in figure 15(a) for $y/\delta_{95} > 0.2$, the turbulent production is actually smaller than the profiles without high free-stream turbulence, also noted by Stefes & Fernholz (2004). Since this is the main source term in the streamwise Reynolds stress equation (defined in (6.1)), this seems counter-intuitive. However, note the velocity profiles in inner variables (figure 6), which show the reduction of the wake region and a smearing of the velocity profiles in the outer region. Thus, the mean velocity gradient is significantly reduced causing a reduction in the turbulent production of $\langle u^2 \rangle$. This means that this term is not responsible for the increased streamwise Reynolds stress, and the high free-stream turbulence has another mechanism for accomplishing this, as will be discussed in §6.2.

The production of $-\langle uv \rangle$ is shown in figure 15(b). Again, using the scaling with u_τ^3/δ_{95}, an insignificant difference exists between the smooth and rough $-\langle uv \rangle$ profiles and the production term $-P_{12}$. However, there is a significant reduction of the turbulence production for the case with free-stream turbulence, for $0.2 < y/\delta_{95} < 1.0$; yet differences in the $-\langle uv \rangle$ profiles with and without free-stream turbulence exist only for $y/\delta_{95} > 0.7$. Again, this indicates different mechanisms in the Reynolds shear stress equation (defined in (6.2)), when high free-stream turbulence is present. To better understand these mechanisms, the discussion of the turbulent diffusion follows in the next section.

6.2. *Turbulent diffusion*

In this section, some important third-order moments are presented to better understand the effects of turbulent transport mechanisms in the presence of free-stream turbulence intensity and roughness. In Antonia & Krogstad (2001) and Andreopoulos & Bradshaw (1981), the velocity triple products have been shown to be more sensitive to the rough surface boundary condition than the second-order moments. As before, the profiles are normalized with the friction velocity u_τ^3 and are shown in figures 16–19. The estimated uncertainty in the triple correlations is expected to be approximately 12 %–18 % depending on wall proximity and component.

Figure 16(a) shows the $\langle u^3 \rangle$ profiles, which represent the streamwise transport of the streamwise Reynolds stress. The importance of this term towards the balance of the $\langle u^2 \rangle$ Reynolds stress equation is minor, since this term enters only through its streamwise gradients (i.e. $\partial/\partial x$) which is small in ZPG flows, and does not appear

(*a*) Production of stream-wise Reynolds stress

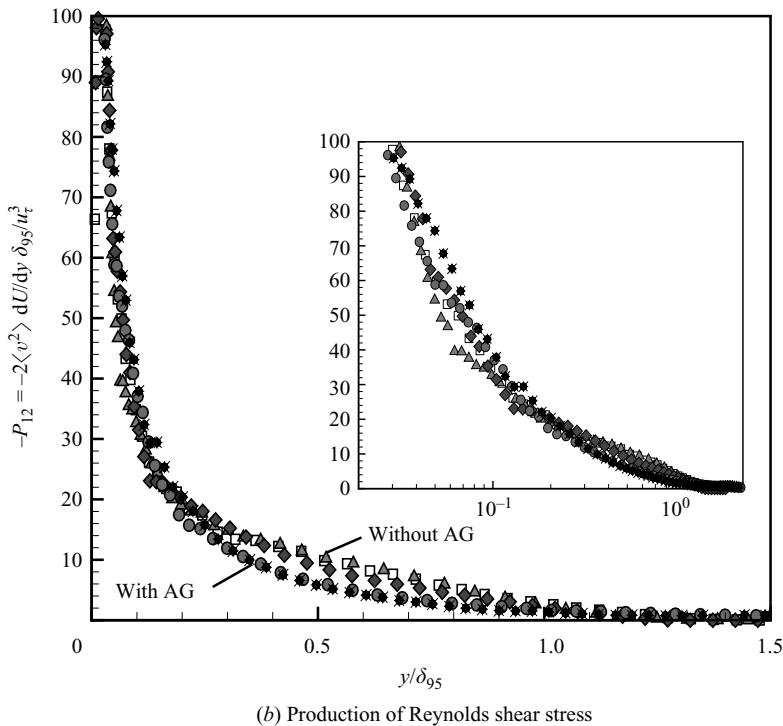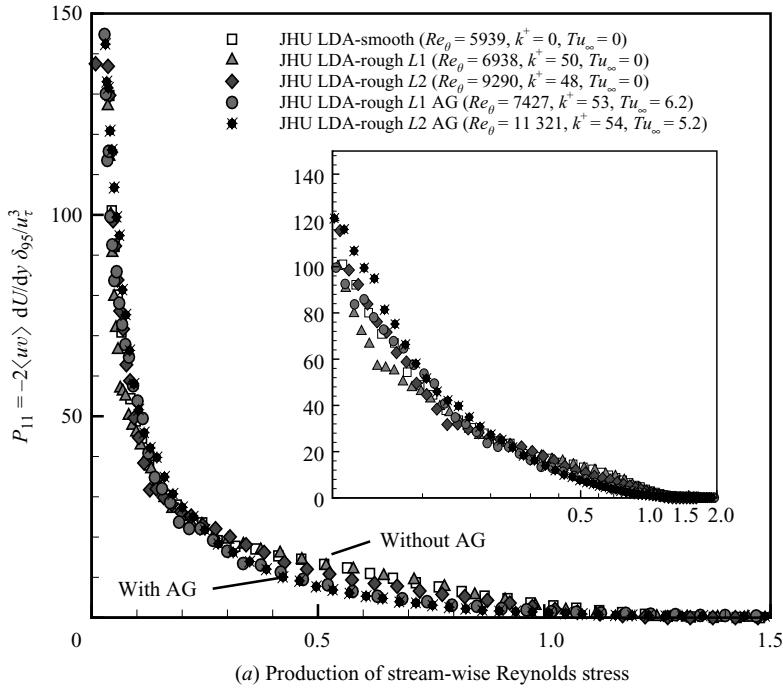(*b*) Production of Reynolds shear stress

FIGURE 15. Measured profiles of turbulent production.

in (6.1). Still, $\langle u^3 \rangle$ may be used to characterize the structure of turbulence and thus the measured results are presented here for completeness. In outer variables, Schultz & Flack (2007) showed that deviations due to roughness are not evident in the $\langle u^3 \rangle$ profiles in the outer region. This is confirmed from the present results, where deviations
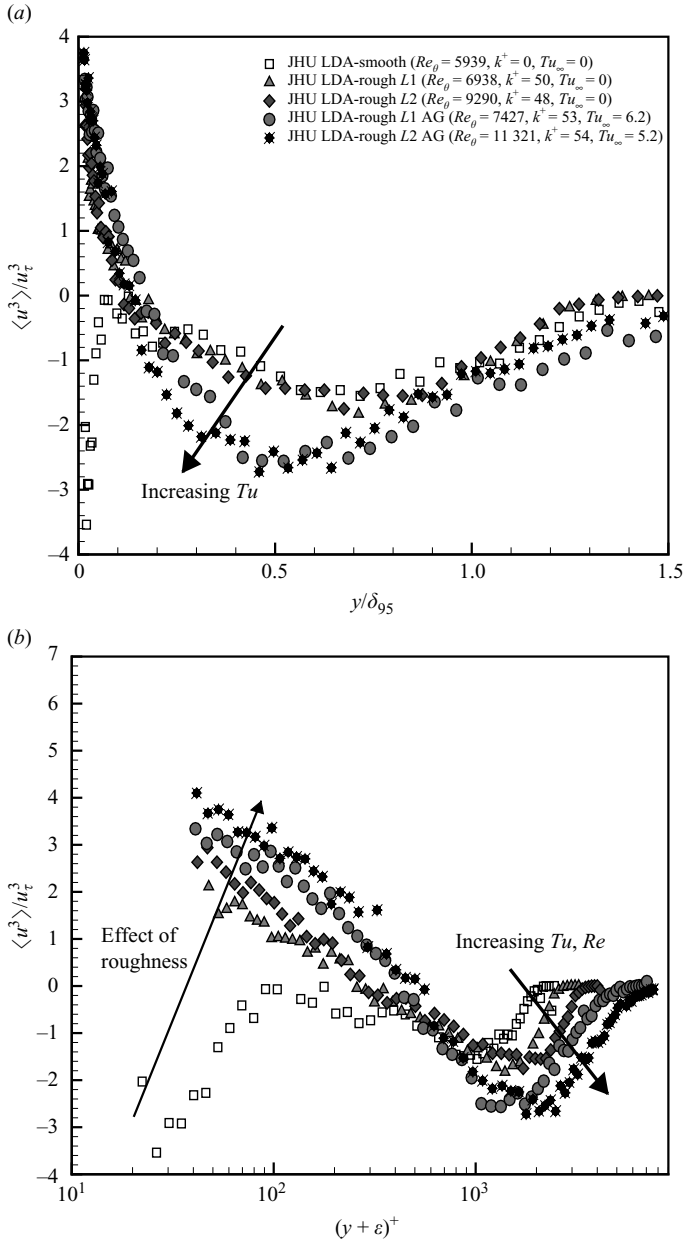
FIGURE 16. Stream-wise flux of the streamwise Reynolds stress, $\langle u^3 \rangle$.

due to roughness are insignificant. However, it is clear that the high free-stream turbulence intensity has a significant effect on the majority of the outer boundary layer, (i.e. $0.1 < y/\delta_{95} < 1.0$). The $\langle u^3 \rangle$ profiles decrease to zero in the turbulent free-stream region beyond $y/\delta_{95} > 1.5$.

The $\langle u^3 \rangle$ profiles in inner variables, are presented in figure 16(b). Schultz & Flack (2007) showed that near the wall, the smooth wall cases display negative values of $\langle u^3 \rangle$, while the profiles over rough surfaces have a positive value. Clearly, this trend is confirmed by present results. Notice that the effect of the free-stream turbulence

does not significantly alter the shape of the $\langle u^3 \rangle$ profiles near the wall, except for an increase in magnitude below $(y + \epsilon)^+ < 400$.

Since $\langle u^3 \rangle$ does not strongly affect the Reynolds stress budget of $\langle u^2 \rangle$, the most likely term is the wall-normal gradients of the $\langle u^2 v \rangle$ profiles. The pressure strain rate is not expected to be a source term in this case either, since the boundary layer is dominated by streamwise fluctuations (i.e. highly anisotropic). Thus, the pressure strain rate is expected to act as a sink term, redistributing the streamwise fluctuation to the $\langle v^2 \rangle$ and $\langle w^2 \rangle$ components (which do not have a turbulent production term). The wall-normal flux of the streamwise Reynolds stress $\langle u^2 v \rangle$ is examined next. It is shown in figure 17(*a*) and does not exhibit significant changes due to roughness in the outer layer. However, a significant effect, i.e. increase, associated with free-stream turbulence is visible throughout the outer region of the boundary layer, as well as extending well into the free-stream. The larger values of the $\langle u^2 v \rangle$ profiles indicate that the addition of free-stream turbulence increases the efficiency of transporting $\langle u^2 \rangle$ across the wall-normal direction. Unfortunately, given the scatter in the triple correlation profiles in general, we are unable to accurately compute the gradients needed to more accurately determine the degree to which this term is responsible for the large increase in the $\langle u^2 \rangle$ budget.

In inner variables, the results are shown in figure 17(*b*). It is clear that roughness alters the direction of the turbulent diffusion, which has a different sign near the wall. However, no significant differences exist due to the free-stream turbulence near the wall.

Figure 18(*a*) shows $\langle u v^2 \rangle$, the wall-normal transport of the Reynolds shear stress in outer variables. Similar to the previous component, in the outer layer, differences occur due to the free-stream turbulence but not due to roughness. These differences, however, are smaller. Figure 18(*a*) shows that the wall-normal gradients of the profiles with high free-stream turbulence are significantly steeper below $y/\delta_{95} < 0.5$ than the profiles without high free-stream turbulence indicating the increased transport of Reynolds shear stress $-\langle uv \rangle$ away from the wall. However, there is no increase in the $-\langle uv \rangle$ profiles below $y/\delta_{95} < 0.5$. This indicates that one of the other terms affects this region, such as the pressure strain term or the pressure velocity correlation. These terms, unfortunately, could not be measured experimentally. It is also important to notice that the production term in the Reynolds shear stress equation is actually a sink term, as well. In inner variables, the triple moment $\langle u v^2 \rangle$ shown in figure 18(*b*) indicates similar results to the $\langle u^2 v \rangle$ profiles. The different sign near the wall is a result of roughness, and no significant differences are seen due to the influence of the high free-stream turbulence in the inner region.

The $\langle v^3 \rangle$ triple moment, shown in figure 19(*a*) in outer units and in figure 19(*b*) in inner units, show significant statistical scatter. However, within the scatter essentially no clear effects of roughness or free-stream turbulence are evident. For a roughness similar to the one in the present experiment, Schultz & Flack (2007) also did not observe deviations due to roughness for this third-order moment. However, Antonia & Krogstad (2001) showed opposite trends in the inner region for this turbulent transport term when comparing two-dimensional rods and a three-dimensional mesh surface.

7. Conclusions

Measurements were performed to study the combined effects of surface roughness and free-stream turbulence on the turbulent boundary layer. At relatively high
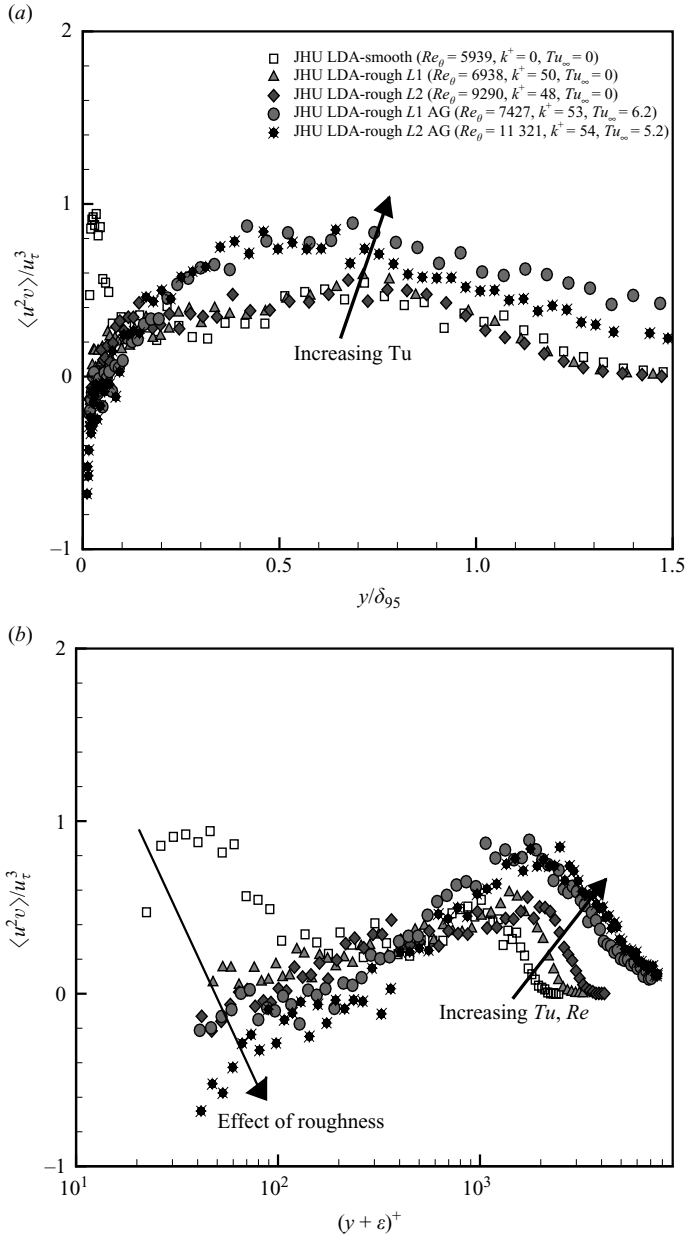
FIGURE 17. Vertical flux of the streamwise Reynolds stress $\langle u^2 v \rangle$.

Reynolds numbers, (i.e. $6000 < Re_\theta < 11\,300$) these measurements provided new data documenting mean velocity, second- and third-order moments in inner and outer variables, as well as a scale-dependent analysis using structure functions. The free-stream turbulence was generated through the use of an active grid which resulted in levels of turbulence intensity of $Tu_\infty = 6.2\,\%$ and $Tu_\infty = 5.2\,\%$ at two downstream locations. As is well known, the effect of the surface roughness is to increase the skin friction coefficient when compared to smooth surfaces. Free-stream turbulence also increases the skin friction 24.5 % and 15.6 % for locations $L1$ ($Tu_\infty = 6.2\,\%$) and
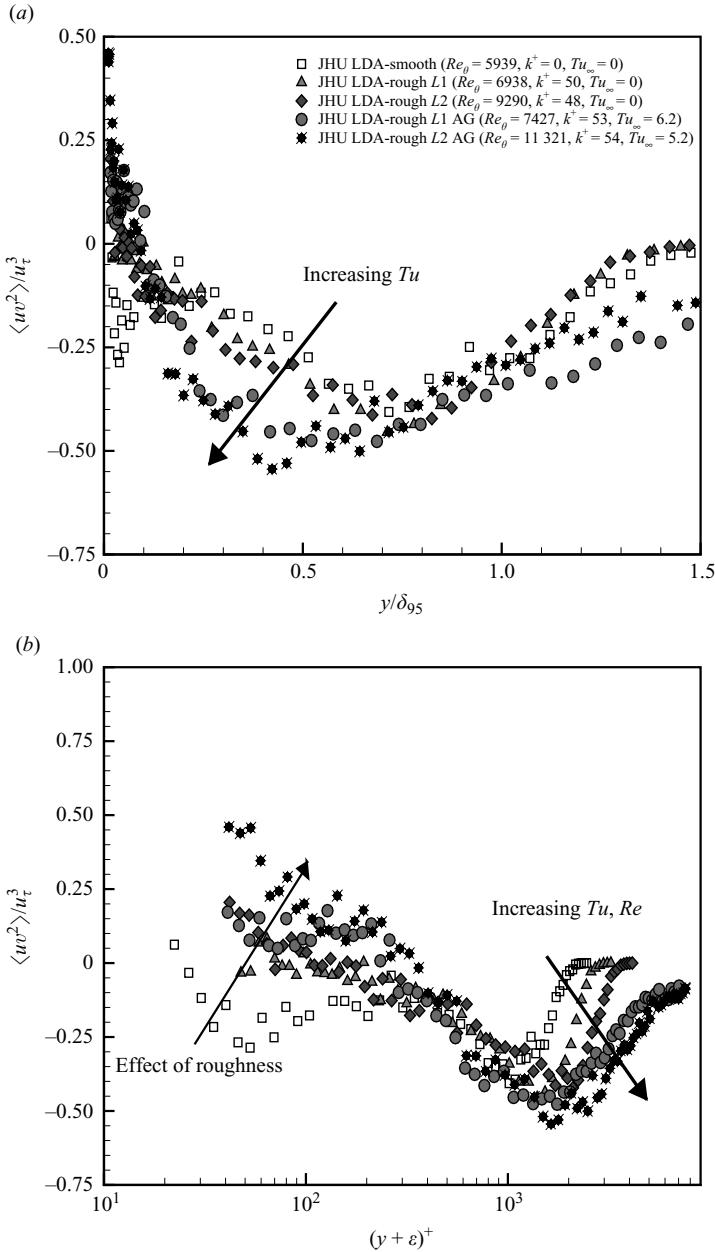
(a)

(b)

FIGURE 18. Vertical flux of the Reynolds shear stress $\langle uv^2 \rangle$.

$L2$ ($Tu_\infty = 5.2\%$), respectively. This is attributed to a higher velocity gradient at the wall for smooth surfaces mainly due to increased momentum flux towards the wall. In rough surfaces, this increase is likely due to an increase in form drag, since the viscous stress contribution decreases with k^+ and increasing Reynolds number δ^+.

Free-stream turbulence alters the velocity profiles for the two scaling techniques examined. In outer variables, using the classical scaling u_τ and the Zagarola & Smits (1998) scaling $U_\infty \delta^*/\delta$, the smooth and rough mean velocity profiles do not show significant differences. However, the effect of high free-stream turbulence is
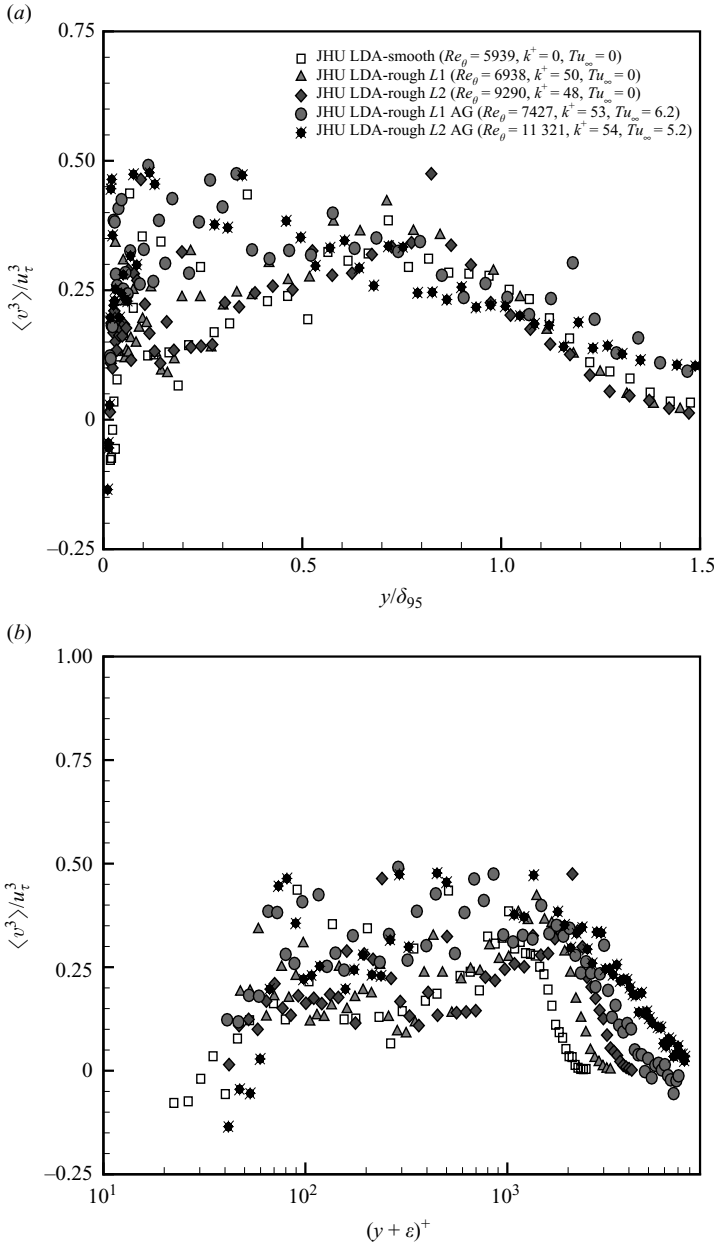
FIGURE 19. Vertical flux of the wall-normal Reynolds stress $\langle v^3 \rangle$.

evident in the wake region and is significantly reduced. Consequently, the classical law of the wake given by Coles (1962) is no longer valid and in real flows, alternate representations are needed. The reduced wake also means that the mean velocity gradient decreases, which reduces the production of the different Reynolds stress components.

The standard boundary layer parameters δ^*/δ_{95} and shape factor H show a significant increase due to surface roughness. However, high free-stream turbulence decreases the parameter δ^*/δ_{95} and shape factor H. The decrease in δ^*/δ_{95} indicates

that the entrainment rate is not proportional to the increased boundary layer thickness. This is consistent with a fuller velocity profile and higher momentum near the wall, which can help prevent separation in cases of adverse pressure gradients. Similarly, the shape factor evolution indicates that free-stream turbulence is not as efficient in mixing, as it is in increasing drag. Both surface roughness and free-stream turbulence increase the boundary layer growth when compared with the smooth surface results.

The streamwise variance (negative Reynolds stress) profiles $\langle u^2 \rangle$ for smooth and rough surfaces collapse well using the classical scaling u_τ^2. Conversely, the effect of the free-stream turbulence augments the streamwise fluctuations significantly throughout the boundary layer, down to at least $y/\delta_{95} \sim 0.07$. By analysing the streamwise Reynolds stress equation, it can be shown that the $\langle u^2 v \rangle$ triple product is the term responsible for the increase in the $\langle u^2 \rangle$ profiles. This can be concluded since the production is in fact reduced due to free-stream turbulence, and the pressure strain term is expected to act as a sink term. This indicates that free-stream turbulence increases the efficiency of transporting the turbulent kinetic energy in the wall-normal direction.

Unlike the streamwise component, free-stream turbulence does not penetrate through the entire $\langle v^2 \rangle$ profile. This is likely due to the pressure fluctuations in the wall-normal direction. Also, in the inner region displayed using inner scaling, neither the $\langle v^2 \rangle$ nor the $-\langle uv \rangle$ profiles show much effects of roughness. The wall-normal and streamwise gradients of the triple correlations $\langle uv^2 \rangle$, as well as the production terms help us understand the differences in turbulent transport, when high free-stream turbulence is present. While in the inner region, the free-stream turbulence does not show significant penetration, the rough surface alters the direction of the turbulent fluxes near the wall.

The different effects of free-stream turbulence on the streamwise and wall-normal variances result in the noteworthy situation that addition of isotropic turbulence in the free-stream promotes anisotropy in the body of the boundary layer. This increase of anisotropy occurs over the wide range from $y/\delta_{95} \sim 0.07$ up to $y/\delta_{95} \sim 0.7$. Second-order structure function analysis shows that these effect of free-stream turbulence are strictly limited to the largest scales of the flow, in a range between $r/\delta_{95} = 3$ and 10.

REFERENCES

AKINLADE, O. G., BERGSTROM, D. J., TACHIE, M. F. & CASTILLO, L. 2004 Outer flow scaling of smooth and rough wall turbulent boundary layers. *Exp. Fluids* **37**, 604–612.

ANDREOPOULOS, J. & BRADSHAW, P. 1981 Measurements of turbulence structure in the boundary layer on a rough surface. *Bound. Layer Meteorol* **20**, 201–213.

ANTONIA, R. A. & KROGSTAD, P. Å. 2001 Turbulence structure in boundary layers over different types of surface roughness. *Fluid Dyn. Res.* **28**, 139–157.

ARONSON, D., JOHANSSON, A. & LÖFDAHL, L. 1996 Shear-free turbulence near a wall. *J. Fluid Mech.* **338**, 363–385.

BANDYOPADHYAY, P. R. 1992 Reynolds number dependence of the free-stream turbulence effects on turbulent boundary layers. *AIAA J.* **30** (7), 1910–1912.

BARRETT, M. J. & HOLLINGSWORTH, D. K. 2003a Correlating friction velocity in turbulent boundary layers subjected to free-stream turbulence. *AIAA J.* **41**, 8, 1444–1451.

BARRETT, M. J. & HOLLINGSWORTH, D. K. 2003b Heat transfer in turbulent boundary layers subjected to free-stream turbulence–Part 1: experimental results. *J. Turbomach.* **125**, 232–241.

BARRETT, M. J. & HOLLINGSWORTH, D. K. 2003c Heat transfer in turbulent boundary layers subjected to free-stream turbulence–Part 2: analysis and correlation. *J. Turbomach.* **125**, 242–251.

BLAIR, M. F. 1983 Influence of free-stream turbuence on turbulent boundary layer heat transfer and mean profile development–Part 2: analysis of results. *J. Heat Transfer* **105**, 41–47.

BRADSHAW, P 2000 A note on 'critical roughness height' and 'transitional roughness'. *Phys. Fluids* **12**, 1611–1614.

BRZEK, B., CAL, R. B., JOHANSSON, G. & CASTILLO, L. 2007 Inner and outer scalings in rough surface turbulent boundary layers. *Phys. Fluids* **19**, 065101.

BRZEK, B., CAL, R. B., JOHANSSON, G. & CASTILLO, L. 2008 Transitionally rough zero pressure gradient turbulent boundary layers. *Exp. Fluids* **44** (1), 115–124.

CAL, R. B., BRZEK, B., JOHANSSON, T. G. & CASTILLO, L. 2008 Influence of external conditions on transitionally rough favorable pressure gradient turbulent boundary layers. *J. Turbulence* **9** (38), 1–22.

CASTILLO, L. 1997 Similarity analysis of turbulent boundary layers. PhD thesis, State University of New York, Buffalo, NY.

CASTILLO, L. & JOHANSSON, G. 2002 The effects of the upstream conditions on a low Reynolds number turbulent boundary layer with zero pressure gradient. *J. Turbul.* **3**, 31, (1–19).

CASTRO, I. 1984 Effects of free stream turbulence on low Reynolds number boundary layers. *J. Fluid Mech.* **585**, 469–485.

CASTRO, I. 2007 Rough wall boundary layers: mean flow universality. *J. Fluids Engng* **106**, 298–306.

CLAUSER F. H. 1954 Turbulent boundary layers in adverse pressure gradients. *J. Aero. Sci.* **21**, 91–108.

COLES, D. E. 1962 Turbulent boundary layers in a compressible fluid. *Tech. Rep.* R-403-PR. RAND Corporation, Santa Monica, CA.

COMTE-BELLOT, G. & CORRSIN, S. 1966 The use of a contraction to improve the isotropy of grid-generated turbulence. *J. Fluid Mech.* **25**, 657–682.

DEGRAAFF, D. B. & EATON, J. K. 2000 Reynolds-number scaling of the flat-plate turbulent boundary layer. *J. Fluid Mech.* **422**, 319–346.

DEGRAAFF, D. B. & EATON, J. K. 2001 A high-resolution laser Doppler anemometer: design, qualification, and uncertainty. *Exp. Fluids* **30**, 522–530.

GEORGE, W. K. 1990 Governing equations, experiments and the experimentalist. *Exp. Therm. Fluid Sci.* **3**, 557–566.

GEORGE, W. K. & CASTILLO, L. 1997 Zero-pressure gradient turbulent boundary layer. *Appl. Mech. Rev.* **50** (12), Part 1, 689–729.

HANCOCK, P. E. & BRADSHAW, P. 1983 The effect of free-stream turbulence on turbulent boundary layers. *J. Fluids Engng* **105**, 284–289.

HANCOCK, P. E. & BRADSHAW, P. 1989 Turbulence structure of a boundary layer beneath a turbulent free-stream. *J. Fluid Mech.* **205**, 45–76.

JIMÉNEZ, J. 2004 Turbulent flows over rough walls. *Annu. Rev. Fluid Mech.* **36**, 173–196.

JOHANSSON, G. & CASTILLO, L. 2002 Near-wall measurements in turbulent boundary layers using Laser Doppler Anemometry. In *Proceedings of the FEDSM2002 – 31070,* Montreal, Canada.

KALTER, M. & FERNHOLZ, H. H. 2001 The reduction and elimination of a closed separation region by free-stream turbulence. *J. Fluid Mech.* **446**, 271–308.

KANG, H. S., CHESTER, S. & MENEVEAU, C. 2003 Decaying turbulence in an active-grid-generated flow and comparisons with large-eddy simulation. *J. Fluid Mech.* **480**, 129–160.

KROGSTAD, P.-Å. & ANTONIA, R. A. 1999 Surface roughness effects in turbulent boundary layers. *Exp. Fluids* **27**, 450–460.

KROGSTAD, P.-Å., ANTONIA, R. A. & BROWNE, L. W. B. 1992 Comparison between rough- and smooth-wall turbulent boundary layers. *J. Fluid Mech.* **245**, 599–617.

LEONARDI, S., ORLANDI, P., SMALLEY, R. J., DJENIDI, L. & ANTONIA, R. A. 2003 Direct numerical simulations of turbulent channel flow with transverse square bars on one wall. *J. Fluid Mech.* **491**, 229–238.

LIGRANI, P. M. & MOFFAT, R. J. 1986 Structure of transitionally rough and fully rough turbulent boundary layers. *J. Fluid Mech.* **162**, 69–98.

MYDLARSKI, L. & WARHAFT, Z. 1996 On the onset of high Reynolds number grid generated wind tunnel turbulence. *J. Fluid Mech.* **320**, 331–368.

MONIN, A. S. & YAGLOM, A. M. 1971 *Statistical Fluid Mechanics* (ed. John L. Lumley). MIT Press.

ÖSTERLUND, J. 1999 Experimental studies of zero pressure-gradient turbulent boundary layer flow. PhD thesis, Royal Institute of Technology, Stockholm, Sweden.

PERRY, A. E. & LI, J. D. 1990 Experimental support for the attached-eddy hypothesis in zero-pressure-gradient turbulent boundary layers. *J. Fluid Mech.* **218**, 405–438.

RADOMSKY, R. W. & THOLE, K. A. 2002 Detail boundary layer measurements on a turbine stator vane at elevated free-stream turbulence levels. *J. Turbomach.* **124**, 107–118.

ROBERTS, S. K. & YARAS, M. I. 2005 Boundary layer transition affected by surface roughness and free-stream turbulence. *J. Fluids Engng* **127**, 449–457.

SCHULTZ, M. P. & FLACK, K. A. 2003 Turbulent boundary layers over surfaces smoothed by sanding. *J. Fluids Engng* **125**, 863–870.

SCHULTZ, M. P. & FLACK, K. A. 2005 Outer layer similarity in fully rough turbulent boundary layer. *Exp. Fluids* **38**, 324–340.

SCHULTZ, M. P. & FLACK, K. A. 2007 The rough wall turbulent boundary layer from the hydraulically smooth to the fully rough regime. *J. Fluid Mech.* **580**, 381–405.

SEO, J., CASTILLO, L., JOHANSSON, G. & HANGAN, H. 2004 Reynolds stress in turbulent boundary layers at high Reynolds number. *J. Turbul.* **5**, 015.

STEFES, B. & FERNHOLZ, H. H. 2004 Skin friction and turbulence measurements in a boundary layer with zero-pressure gradient under the influence of high intensity free-stream turbulence. *Euro. J. Mech.* B/*Fluids* **23**, 303–318.

TACHIE, M. F., BERGSTROM, D. J. & BALACHANDAR 2000 Rough wall turbulent boundary layers in shallow open channel flow. *J. Fluids Engng* **122**, 533–541.

TACHIE, M. F., BERGSTROM, D. J. & BALACHANDAR 2003 Roughness effects in a low-Re_θ open channel turbulent boundary layer. *Exp. Fluids* **35**, 338–346.

THOLE, K. A. & BOGARD, D. G. 1995 Enhanced heat transfer and shear stress due to high free-stream turbulence. *J. Turbomach.* **117**, 418–424.

THOLE, K. A. & BOGARD, D. G. 1996 High free-stream turbulence effects on turbulent boundary layers. *J. Fluids Engng* **118**, 276–844.

TOWNSEND, A. A. 1976 *The Structure of Turbulent Shear Flows*. Cambridge University Press.

ZAGAROLA, M. V. & SMITS, A. J. 1998 Mean-flow scaling of turbulent pipe flow. *J. Fluid Mech.* **373**, 33–79.